Structure of the complete, membrane-assembled COPII coat reveals a complex interaction network.

Joshua Hutchings[1,5], Viktoriya G. Stancheva[2], Nick R. Brown[1,3], Alan C.M. Cheung[1,4], Elizabeth A. Miller[2] and Giulia Zanetti*[1].

[1]Institute of Structural and Molecular Biology, Birkbeck College, London

[2]MRC Laboratory of Molecular Biology, Cambridge

[3]Present address: The Francis Crick Institute, London

[4]Present address: School of Biochemistry at the University of Bristol

[5]Present address: Division of Biological Sciences, University of California San Diego, La Jolla, CA

*correspondence: g.zanetti@bbk.ac.uk

Abstract

The COPII coat mediates Endoplasmic Reticulum (ER) to Golgi trafficking for thousands of proteins. Five essential coat proteins assemble at the ER into a characteristic two-layer architecture, which recruits cargo proteins whilst sculpting membrane carriers with diverse morphologies. How coat architecture drives membrane curvature whilst ensuring morphological plasticity is largely unknown, yet is central to understanding mechanisms of carrier formation. Here, we use an established reconstitution system to visualise the complete, membrane-assembled COPII coat with unprecedented detail by cryo-electron tomography and subtomogram averaging. We discover a network of interactions within and between coat layers, including multiple interfaces that were previously unknown. We reveal the physiological importance of these interactions using genetic and biochemical approaches. A newly resolved Sec31 C-terminal domain provides order to the coat and is essential to drive membrane curvature in cells. Moreover, a novel outer coat assembly mode provides a basis for coat adaptability to varying membrane curvatures. Furthermore, a newly resolved region of Sec23, which we term the L-loop, imparts coat stability and in part dictates membrane shape. Our results suggest these interactions collectively contribute to coat organisation and membrane curvature, providing a structural framework to understand regulatory mechanisms of COPII trafficking and secretion.

Introduction

Eukaryotic cells are organized in membrane-bound compartments, and a tightly regulated trafficking system ensures proteins and lipids are delivered to the right place at the right time. Cytosolic coat proteins capture secretory cargo and sculpt membrane carriers for intracellular transport (Bonifacino and Glick, 2004). A third of all proteins in eukaryotic cells are synthesized in the Endoplasmic Reticulum (ER) and trafficked to the Golgi, destined for secretion or residency within organelles (Ghaemmaghami et al., 2003). ER export is mediated by the coat protein complex II (COPII), which minimally comprises five cytosolic proteins that form two concentric layers on the ER membrane – the inner and outer coat (Zanetti et al., 2012). The inner coat layer consists of the small GTPase Sar1 and the heterodimeric Sec23/24 complex, whilst the outer coat layer comprises the rod-shaped heterotetramer Sec13/31. COPII dynamically assembles and disassembles at ER exit sites, imparting enough force to bend the membrane into unfavourable conformations while at the same time maintaining a range of membrane curvatures. It remains unclear how the COPII coat achieves the required balance of strength and flexibility, and how this balance is regulated to form vesicles of different sizes and shapes, essential to transport a diverse range of cargo molecules (Hutchings and Zanetti, 2019).

COPII assembly begins with the formation of the inner coat, after GTP-bound Sar1 exposes an amphipathic helix for burial into the ER membrane (Hutchings et al., 2018; Lee et al., 2005). Sar1-GTP then recruits Sec23/24. Sec23 binds Sar1 and is the dedicated GTPase-activating protein (GAP)

(Antonny et al., 2001; Barlowe et al., 1994; Bi et al., 2002), whilst Sec24 possesses multiple binding sites for cargo recruitment (Miller et al., 2003; Mossessova et al., 2003). Sec23 also recruits the outer coat subunits Sec13/31 through a flexible proline-rich domain (PRD) in the C-terminal half of Sec31, which accelerates the GAP activity of Sec23 (Bi et al., 2007). Both the inner and the outer coat are thought to oligomerise and induce membrane curvature to form coated membrane carriers (Hutchings et al., 2018; Stagg et al., 2008, 2006; Zanetti et al., 2013). COPII has been shown to generate vesicles and tubules both *in vivo* and *in vitro*, suggesting the coat is adaptable for different morphologies (Bacia et al., 2011; Barlowe et al., 1994; Fromme et al., 2007; Gorur et al., 2017; K. Matsuoka et al., 1998; Venditti et al., 2012; Zanetti et al., 2013). This is consistent with a need to maintain constitutive secretion of soluble proteins, whilst also accommodating much larger cargo such as procollagens and pre-chylomicrons in specialised mammalian cells (Gorur et al., 2017; Hutchings and Zanetti, 2019; Jin et al., 2012; Malhotra and Erlmann, 2015; Townley et al., 2008).

COPII assembly is governed by numerous interactions within and between the coat layers (Bi et al., 2007; Hutchings et al., 2018; Ma and Goldberg, 2016; Stagg et al., 2008; Stancheva et al., 2020). Lateral interactions between inner coat subunits mediate its polymerisation into arrays, which have been proposed to prime coat assembly and directly orient membrane curvature through Sar1 amphipathic helix insertion (Hutchings et al., 2018). The outer coat proteins Sec13/31 also self-associate, assembling into cages of different geometries *in vitro*, including polyhedral and tubular arrangements of varying diameters (Stagg et al., 2008, 2006; Zanetti et al., 2013). The assembly units of the cage comprise two structured domains in the N-terminal half of Sec31: an N-terminal β-propeller and an α-solenoid domain. These domains are separated by a blade insertion motif, which binds the Sec13 β-propeller and rigidifies the assembly (Čopič et al., 2012; Fath et al., 2007). The Sec31 α-solenoid domain drives homodimerisation of Sec31 to create a rod-shaped tetrameric assembly element, whilst the N-terminal β-propeller domain mediates contacts between four rods to generate a cage (Fath et al., 2007). Sec31 also contains a putative helical C-terminal domain (CTD), that is separated from the cage-forming elements by a long flexible proline-rich domain (PRD) (Fath et al., 2007). No role for the CTD has yet been assigned, but limited proteolysis experiments and secondary structure prediction suggest an ordered helical domain of ~18 kDa (Dokudovskaya et al., 2006; Paraan et al., 2018).

Interactions between inner and outer coat layers are mediated by the Sec31 PRD, which binds Sec23 at several interfaces, including: i) a GAP-accelerating region that binds the Sar1-Sec23 interface (Bi et al., 2007), ii) triple-proline (PPP) motifs binding the tip of the Sec23 gelsolin domain that assist in the assembly of inner coat subunits (Hutchings et al., 2018; Ma and Goldberg, 2016), and iii) a recently defined but structurally uncharacterized charge-based interaction (Stancheva et al., 2020). Several COPII ancillary proteins also possess PRDs that bind Sec23 in a similar way to Sec31, possibly stabilising the coat for formation of larger carriers during procollagen transport in mammals (Hutchings and Zanetti, 2019; Ma and Goldberg, 2016; Saito et al., 2009; Santos et al., 2016). Some of the interaction interfaces, including outer-inner coat interactions mediated by PPP motifs and the Sec31 active peptide, as well as cage vertices, have been characterized structurally. Disruption of many of these interfaces are tolerated individually but not in combination, implying a network of partially redundant interactions that collectively stabilise coat assembly (Hutchings et al., 2018; Stancheva et al., 2020). For instance, partial disruption of outer coat polymerisation by means of an N-terminal His-tag on Sec31 (NHis-Sec31) still permits viability in yeast, but not in combination with other mutations targeting PRD interactions (Stancheva et al., 2020).

The full extent and role of coat interactions is not clear, and several questions remain unanswered. How does the interplay between inner and outer coat layers influence membrane curvature and budding morphology? Which coat interactions have a regulatory role? Which interactions are important to provide membrane bending force, and which confer flexibility to the coat? Here, we build on a previously established approach (Hutchings et al., 2018; Zanetti et al., 2013) using cryo-electron tomography (cryo-ET) and subtomogram averaging (STA) of *in vitro* reconstituted COPII coated tubules to obtain the complete, detailed picture of a fully assembled wild-type coat. In addition to structurally

characterising known interactions to unprecedented detail, we describe novel ones that link both coat layers into an intricate network.

At the level of the outer coat, we describe a vertex interface that is significantly different from previous reports, we discover an essential role for the structurally and functionally elusive Sec31 CTD as a key node of the COPII network, and an unexpected interaction between Sec31 β-propeller and α-solenoid domains that seems to confer the ability to adapt to membrane with varying curvatures. We map three different interactions between the inner and outer coat layers, including a structurally uncharacterised charged interaction that was recently identified through biochemical and genetic analysis (Stancheva et al., 2020). Finally, at the inner coat assembly interface we resolve a novel flexible loop on Sec23 that becomes ordered to contribute to lattice formation. We include biochemical and genetic analyses that shed light on the role of many of known and novel interactions, providing evidence for a complex and flexible network that serves as a basis for dynamic regulation of membrane remodelling.

Results

Detailed architecture of outer coat vertices suggests conditional requirement for vertex formation

Incubating purified COPII components with GUVs and non-hydrolysable GTP (GMP-PNP) induces extensive tubulation of membranes (Bacia et al., 2011; Zanetti et al., 2013). We optimised our previously established *in vitro* reconstitution and structural analysis pipeline (Hutchings et al., 2018; Zanetti et al., 2013) to obtain high-resolution cryo-EM data of COPII induced tubules. We collected tilt series of reconstituted budding reactions, which were subsequently used to reconstruct 3D tomograms of the tubules (Fig 1 A and Supplementary Fig 1A), and we then used subtomogram averaging to obtain the structures, positions and orientations of inner and outer coat subunits (Methods and Supplementary Fig 1B,D).

The outer coat forms a sparse rhomboidal lattice in which four Sec31 N-terminal β-propeller domains interact to form 2-fold symmetric X-shaped vertices (Fig. 1B,C). The vertex was refined to a resolution of approximately 12 Å (Supplementary Fig. 2A). We could clearly distinguish the β-propeller shapes and unambiguously rigid-body fit the available Sec13/31 crystal structures (Fig. 1C). The Sec13 β-propeller is also clearly defined, although features gradually degrade along rods further from the vertex, probably due to a higher degree of flexibility. Close analysis of the vertex β-propeller interfaces identified a region of density that likely corresponds to a negatively charged loop (residues 339-357: EQETETKQQESETDFWNNV) that is disordered in the crystal structure (Fath et al., 2007). It appears that this loop becomes ordered in the assembled vertex and forms an interaction interface with the neighbouring subunits (Supplementary Fig. 3A). We previously discovered that Sec31 with a his-tag at its N-terminus (Nhis-Sec31) yielded tubes with a disordered outer coat, due to destabilization of vertex formation (Hutchings et al., 2018). The proximity of the 339-357 loop to the N-terminus of Sec31 might explain the vertex disruption we observed with Nhis- Sec31 (Hutchings et al., 2018), as the tag might displace or interfere with this interaction surface.

With this new insight into how Nhis-Sec31 might perturb cage assembly, we sought to further probe the importance of vertex interactions by disrupting the system even further and deleting the Sec31 N-terminal β-propeller domain (residues 1-372, Sec31-ΔNTD, Figure 1D, top panel). Abrogating outer coat vertex interactions completely did not support vesicle formation from microsomes, even with the coat stabilised by non-hydrolysable GTP analogs, a condition that was permissive for Nhis-Sec31 (Hutchings et al., 2018)(Supplementary Fig. 3B). Sec31-ΔNTD was efficiently recruited to membranes (Supplementary Fig. 3C), and, surprisingly, was capable of tubulating GUVs, suggesting its ability to organize the inner coat array was intact, and that inner coat organization is sufficient to drive membrane curvature in a synthetic model membrane (Supplementary Fig. 3D). Sec31-ΔNTD was lethal when expressed as the sole copy of Sec31 in wild-type yeast (Fig. 1D, middle panel), but was viable in an *emp24Δ* strain (Fig 1D, bottom panel). Deletion of Emp24 is thought to lower the membrane bending energy during vesicle formation by depleting abundant lumenally-oriented cargo. This condition has

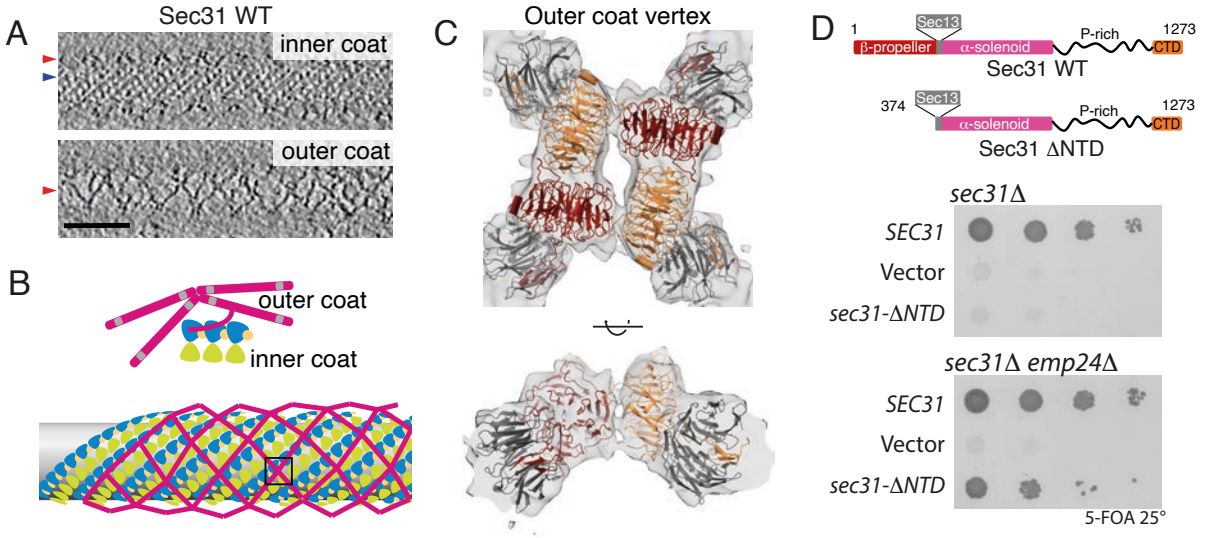

Figure1. Architecture of outer COPII coat vertices

A. Slices through different z heights of a binned and filtered representative cryo-tomogram of wild type COPII-coated tubule. Inner and outer coats (blue and red arrowheads respectively) are visible. Scale bar 50 nm.

B. Schematic representation of outer coat architecture. Sec13-31 subunits arrange in a lozenge pattern, around the inner coat that arranges in a tightly packed lattice. Panels C-E focus on the structure of vertices, boxed in this schematics.

C. Top and side views of the 12 Å subtomogram average of the COPII vertex, with rigid-body fitted atomic models (PDB 2PM6 and 2PM9). Sec31 protomers in dark red and orange, Sec13 in gray.

D. Top panel: Domain organisation of wild type Sec31, and the ΔNTD mutant. Middle panel: a *sec31Δ* yeast strain transformed with the indicated plasmids was tested on 5-FOA, revealing lethality associated with deletion of the NTD. Bottom panel: the same experiment repeated with a *sec31Δ emp24Δ* yeast strain reveals that depletion of emp24 rescues the lethality associated with deletion of the Sec31 NTD.

been shown previously to confer tolerance to the otherwise lethal absence of Sec13 (Čopič et al., 2012). Together, the *in vitro* and *in vivo* phenotypes reveal that outer coat vertex interactions are not needed to generate curvature on easily deformable membranes. This suggests that a main driving force for budding is inner coat lattice formation, and that the stable association of vertex interfaces, as well as inner coat stability tuned by GTPase activity, are needed for remodelling of cargo-containing membranes that resist budding.

Comparison with previously obtained vertex structures

The arrangement of the Sec31 N-terminal β-propellers in our structure differs significantly from previously published cryo-EM single particle reconstructions obtained from human Sec13-31 cages assembled in the absence of a membrane (Noble et al., 2013; Stagg et al., 2008, 2006) (Supplementary Fig. 3E). Indeed, when comparing the soluble cage vertex with that obtained in this study by overlapping one of the Sec31 β-propeller subunits, we find that the relative position of both neighbours is shifted by more than 15Å (Supplementary Fig. 3F). In the soluble cages, a pair of opposite β-propellers in the vertex forms a tight interaction (identifying the '+' contacts (Stagg et al., 2006)), while the other pair is further apart, separated by the '+' rods (and referred to as the '-' interaction). In the context of the membrane-assembled coat, we see a clear gap between both the '+' and '-' pairs of β-propellers (Supplementary Fig. 3E). Multiple effects might cause this difference: 1. Interactions of vertices arranged in a tubular geometry may be different from those on spherical vesicles; 2. Interactions in soluble cages may be distinct from those in the membrane-assembled coat; and 3. Proteins from different species may have evolved different interaction interfaces, while maintaining an overall similar assembly architecture. We tested the first two hypotheses by examining the small populations of spherical vesicles and empty cages that were present in our tomograms. We manually picked vertices

and performed alignments against two different references: one derived from the soluble cage vertex and one from our vertex structure on membrane tubules. For both datasets, alignments converged to virtually identical structures, with an interface similar to that on membrane-assembled tubules, with a clear gap at the centre of the vertex (Supplementary Fig. 4). While we cannot exclude that the difference we see between empty cages in our sample and those previously published might be caused by buffer conditions, we hypothesise that vertex interactions are different in yeast and human.

Detailed structure of interconnecting rods

Outer coat vertices are connected by Sec13-31 rods that wrap tubules both in a left- and right-handed manner, which we refer to as left- and right-handed rods (Zanetti et al., 2013). As mentioned above, when refining by alignment of vertices, the density further from the centre gradually degrades, due to increased flexibility or heterogeneity. We therefore analysed the structure of the interconnecting rods by focusing the refinements at the mid-points between vertices (see Methods). Left-handed rods (Fig. 2A) averaged to a resolution of ~11 Å (Supplementary Fig. 2A), and we could fit the available crystal structures of dimeric edge elements (Fath et al., 2007) by treating each monomer as a rigid body (Fig. 2B,C). At this resolution we can distinguish helical profiles and individual blades of the Sec13 β-propeller (Fig. 2C). As previously reported, rods in membrane-coated tubules are only slightly bent, resembling the X-ray structure (Fath et al., 2007) rather than the highly bent edges of soluble assembled cages (Fig. 2B, bottom panel, (Stagg et al., 2006)). Surprisingly, we detected a previously unresolved extra density attached to the rod halfway between Sec13 and the dimerization interface (Fig. 2B,D). The size of this appendage is indicative of a full domain. This extra density is probably sub-stoichiometric, as we could see it clearly only at low contour levels (Fig. 2B,D) or in averages with lower sharpening levels (not shown). We reasoned that it could correspond to the Sec31 CTD, which is predicted to be a structured helical domain (Dokudovskaya et al., 2006; Fath et al., 2007).

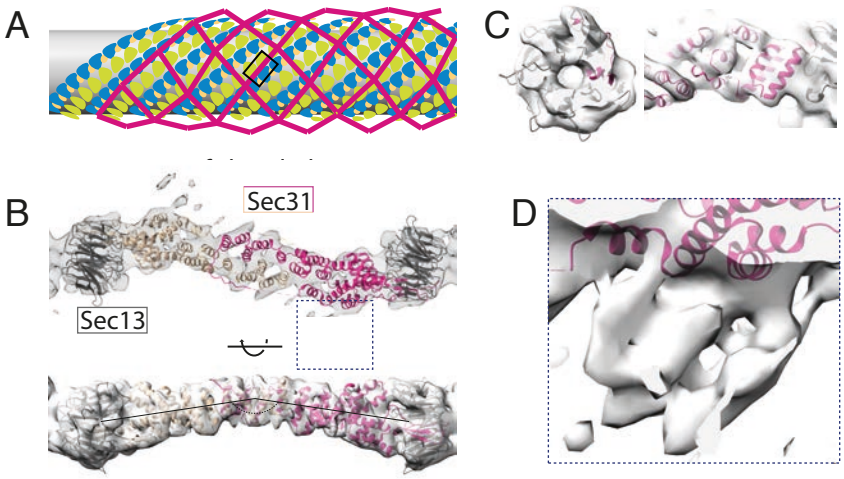

Figure 2. Architecture of COPII rods organised in a left-handed manner

A. Schematic representation of outer coat lozenge architecture, with left-handed rod positions highlighted in the box.

B. Top panel: top view of the 11 Å subtomogram average of the COPII left-handed rod, with rigid-body fitted atomic models (PDB 2PM6). The dimerising protomers are shown in dark and light pink, Sec13 in grey. Bottom panel: sideview of B.

C. Details of the map in B, showing the quality of the fit. Left panel: detail of Sec13 β-propeller. Righ panel: detail of Sec31 α-solenoid domain.

D. Enlargement of the region boxed in panel B shown at lower contour to display an extra density.

Sec31 C-terminal domain mediates essential coat interactions

To confirm that the appendage density corresponds to the CTD of Sec31, we analysed GUVs budded with a truncated form of Sec31 (encompassing residues 1 to 1114, referred to as Sec31-ΔCTD, Fig. 3A). In cryo-tomograms of these tubules the outer coat was generally less ordered with respect to the wild type, whilst the inner coat maintained a typical pseudo-helical lattice (Fig. 3B). To conduct an unbiased search for rods, we used a featureless rod-like structure as a template, and subsequently aligned the detected particles to the subtomogram average obtained from the wild type sample. The average of Sec31-ΔCTD rods recovers the characteristic features and has similar resolution to the wild type rod, but it lacks the appendage density (Fig. 3C, orange arrowhead), confirming this density most likely corresponds to the CTD. The Sec31-ΔCTD rod also showed weaker density for vertices and the inner coat and membrane layer (Fig. 3C, red, blue and beige arrowheads, respectively), indicative of its less ordered arrangement.

Since no atomic model for Sec31 CTD has been determined, we built a homology model to fit into the appendage density. Steroid Receptor RNA Activator protein (SRA1) is the closest homologue to Sec31 CTD for which an atomic structure exists (Bilinovich et al., 2014). SRA1 is a functionally unrelated protein that is found only in mammals, and its evolutionary links with Sec31 are unclear. Nevertheless, SRA1

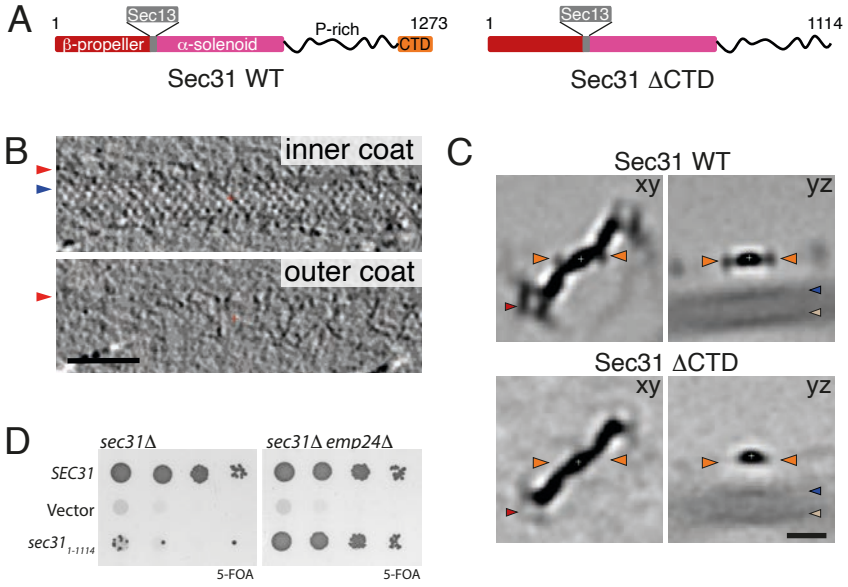

Figure 3. Role of the Sec31 CTD

A. Domain organisation of wild type Sec31, and the ΔCTD mutant.

B. Slices through different z heights of a binned and filtered representative cryo-tomogram of COPII-coated tubule formed with Sec31-ΔCTD. Arrowheads as in Fig. 1A. The outer coat appears partially disordered. Scale bar 50 nm.

C. Top panels: slices through xy and yz planes of 8X binned subtomogram average of rods extracted from wild type tubules. Orange arrowheads indicate the appendage density in Fig 2D. Red arrowhead indicates the vertex, and beige is the membrane. Bottom panels. The same slices for the average of rods extracted from tubules formed with Sec31-ΔCTD. Extra density is absent, confirming its assignment to Sec31 CTD. The density for the vertex and membrane is also fainter, indicating overall disorder of rods in this sample. Scale bar 10 nm.

D. Left panel: a sec31Δ yeast strain transformed with the indicated plasmids was tested on 5-FOA, revealing lethality associated with deletion of the CTD. Right panel: the same plasmids were transformed into a sec31Δ emp24Δ yeast strain revealing rescue of viability.

and Sec31 CTD belong to the same evolutionary family and their similarity justifies the use of the SRA1 structure to build a homology model of the Sec31 CTD (see Methods). Rigid-body fitting the homology model in the appendage density shows consistency of features, and provides insights into the binding orientation of the CTD, although at this resolution we cannot determine the precise molecular interface (Supplementary Fig. 5A-C).

In order to assess the physiological importance of the Sec31 CTD in the secretory pathway, we made yeast mutants where Sec31 was substituted with Sec31-ΔCTD. When the truncated form was the sole copy of Sec31 in yeast, cells were not viable, indicating that the novel interaction we detect is essential for COPII coat function (Fig. 3D, left panel). In contrast, when the cargo burden was decreased by deletion of the ER export receptor, Emp24, Sec31-ΔCTD supported viability (Fig. 3D, right panel). This phenotype is similar to the depletion of the Sec31-ΔNTD or of Sec13 (Čopič et al., 2012), and leads us to hypothesise that Sec31 CTD binding to Sec31 rods stabilises the COPII interaction network, thereby imparting rigidity and strengthening the coat. Microsome budding reconstitution experiments using Sec31-ΔCTD give further insight into this functional defect. The mutant protein is capable of forming vesicles in the presence of a non-hydrolysable GTP analogue, albeit with reduced efficiency compared to wild type. However, when GTP is used, vesicles fail to form despite Sec31-ΔCTD being efficiently recruited to membranes (Supplementary Fig. 5D, E). This indicates that CTD-mediated outer coat stabilisation becomes necessary when inner coat turnover is allowed, reminiscent of the phenotype seen with Nhis-Sec31 and further supporting a role in outer coat organisation (Hutchings et al., 2018).

We next asked whether stabilisation of both the N and C-terminal interactions was dispensable in conditions of efficient inner coat polymerisation, by performing GUV budding reconstitutions in the presence of Nhis-Sec31-ΔCTD. While both Sec31-ΔCTD and Nhis-Sec31 showed tubulation, we could not detect any tubules in negatively stained grids of the combined mutant (data not shown). This suggests that, even when membranes are easily deformable and inner coat assembly is stabilised by the absence of GTP hydrolysis, some level of outer coat organisation is required to deform membranes, and the inner coat bridging activity of the Sec31 triple proline motifs is not sufficient.

Interactions between β-propeller and α-solenoid domains define extra rod connections.

We next analysed rods that interconnect vertices in the right-handed direction (Fig. 4A). Surprisingly, in addition to the CTD appendages, a second region of ill-defined extra density was present near the Sec31 dimerization region (Supplementary Fig. 6A). Upon classification we could divide the right-handed rod dataset into two classes, both of which converged to resolutions between 13 Å and 15 Å (Fig. 4B and Supplementary Fig. 3A). The first class is analogous to the left-handed rods, whereas the second class has a density attached to the centre of the rod which clearly resembles a pair of β-propeller subunits, suggesting the presence of an unexpected additional Sec13-31 edge attached to the Sec31 α-solenoid. We confirmed the nature of the extra density by focussing refinements on the predicted centre of the 'extra' rod, obtaining the unambiguous shape of a Sec13-31 heterotetramer (Supplementary Fig. 6B), which runs nearly perpendicular to, and bridges between, two right-handed rods. Analysis of the averages placed in the context of individual tomograms shows that the extra rods are sparsely and randomly distributed (Fig. 4C). We also note that they follow a similar direction to the left-handed rods, running along the direction of the main Sec23-Sec23 inner coat interfaces (Fig. 4D).

Since the extra rods bridge between α-solenoid dimerization interfaces of right-handed rods, we expect that the distribution of neighbouring vertices compared to the centres of the extra rods should form a rhombus (dotted lines in Supplementary Fig. 6C). However, when we plotted the position of vertices neighbouring the extra rods, we noticed that in addition to the expected peaks, there was a cluster of vertices positioned at the tip of the extra rods (Supplementary Fig. 6C, red circle). This suggested that a subpopulation of these extra rods could connect to a right-handed rod on one side and form a standard vertex on the other. By selecting these rods and calculating their average, we confirmed the presence of the two different connections (Supplementary Fig. 6D). The localisation of these hybrid rods in the tomogram shows that these are often placed at the interface between two patches of outer

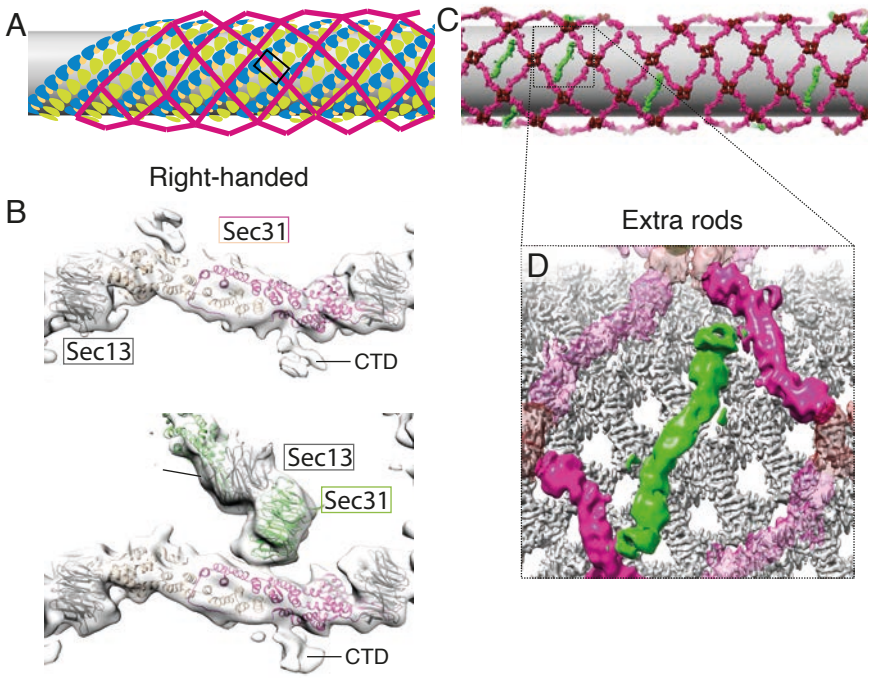

Figure 4. Architecture of COPII rods organised in a right-handed manner

A. Schematic representation of coat architecture, with right-handed rod positions highlighted in the box.

B. Top panel: top view of the 13 Å subtomogram average of the COPII right-handed rod with no extra density at the dimerization interface, with rigid-body fitted atomic models (PDB 2PM9). The dimerising protomers are shown in dark and light pink, Sec13 in grey. The CTD is visible in these rods. Bottom panel: the same view of a class of right-handed rods that displays an attachment of another rod. The Sec13-31 beta propeller tandem is fitted (Sec31 in green and Sec13 in grey).

C. Averages of vertices (dark red), left and right-handed rods (pink) are placed in their aligned positions and orientations in a representative tomogram. Extra rods are placed in green, and display random distribution, but unique orientation.

D. Enlargement of the placed object, with the placed inner coat (grey), showing that extra rods orient roughly parallel to the inner coat lattice direction.

coat lattice that come together with a mismatch (Supplementary Fig. 6E). This indicates that the novel mode of interaction we characterise here might help the outer coat network adapt to different curvatures.

Extended interactions between the inner coat and the Sec31 disordered region.

Compared to previous work (Hutchings et al., 2018), the ordered outer coat now allows to gain new insights into inter-layer interactions. We therefore refined the structure of the inner coat from fully ordered coated tubules to an average resolution of 4.6Å (Supplementary Fig. 2B). Density modification (Terwilliger et al., 2020) and sharpening further improved features in the map (Supplementary Fig. 7A), permitting to unambiguously fit of X-ray models of Sec23, Sec24 and Sar1. The resolution and overall quality of our map allowed us to build regions that were missing from the X-ray structures and refine the model (Supplementary Fig. 7B,C). We analysed the sites of interaction with the outer coat by identifying regions in the map that are not explained by the model (prominent regions in their difference map, Fig. 5A,B). These are generally better defined than in our previous map obtained with disordered outer coat (Hutchings et al., 2018), possibly due to more stable interactions and lower flexibility. We confirmed the binding of the Sec31 active peptide to Sec23 through its WN residues, as well as that of Sec31 PPP motifs to the Sec23 gelsolin domain. Here we can clearly detect a single density that extends on both sides of the prolines to contact two adjacent inner coat subunits,

supporting previous hypotheses that PPP-containing sequences bridge between neighbouring inner coat subunits and contribute to the stability of the lattice (Fig. 5B) (Hutchings et al., 2018; Ma and Goldberg, 2016; Stancheva et al., 2020).

In addition to the expected Sec31 binding sites, the difference map showed a prominent region that we did not see in the context of Nhis-Sec31. We now see density corresponding to a long 'sausage-like' region nestled in a negatively charged concave surface between the Sec23 Zn-finger, helical, and gelsolin-like domains (Fig. 5B, C, asterisk). In a recent report, we showed that binding between the outer and inner layers of the COPII coat is mediated by multivalent interactions of the Sec31 disordered domain with Sec23 (Stancheva et al., 2020). These interactions involve the previously identified catalytic and triple proline regions, and a novel charge-based interaction between the positively charged Sec31 disordered domain and negatively charged surface on Sec23. Charge reversal of the Sec23 surface led to abolished recruitment of Sec13-31 and a non-functional coat (Stancheva et al., 2020). We are now able to map this essential interaction and show it spans ~25 Å, corresponding to 9-10 residues.

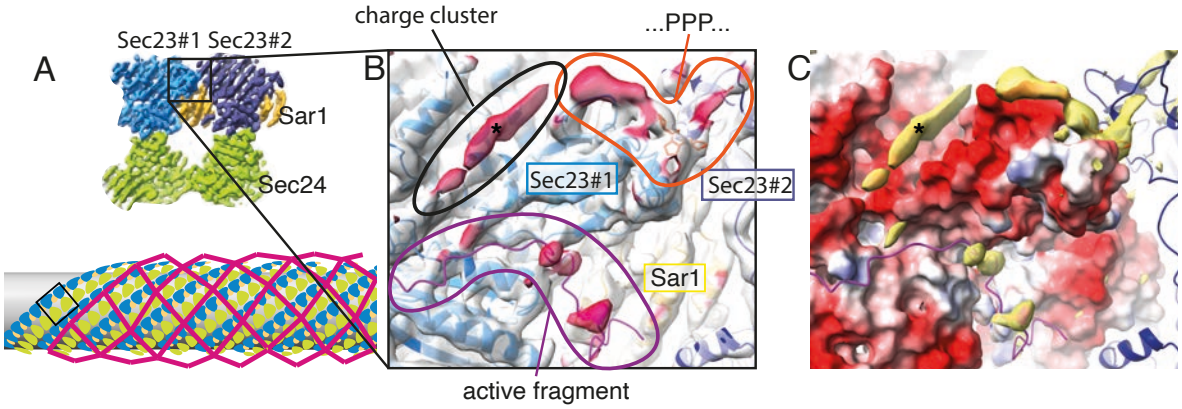

Figure 5. Inner-outer coat interactions

A. Top: the inner coat lattice structure, with a box indicating the region represented in panels B and C. Bottom: schematic representation of coat architecture, with inner coat highlighted in the box.

B. The density-modified inner coat subtomogram average and the refined atomic model. The map is coloured in transparent white, while regions that are further than 3 Å from the model are coloured in dark red, indicating density that is not explained by the model and is attributed to outer coat binding.

C. The difference map between the map and a model-generated density (filtered at 4 Å, yellow) is overlaid to the model surface coloured according to its Coulombic potential. The outer coat density indicated by the asterisk binds to a negatively charged groove on Sec23.

Sec23-Sar1 interactions in lattice formation

Inner coat subunits assemble through a lattice interface between Sar1 and Sec23 from one protomer, and Sec23 from the neighbouring protomer (Fig. 6A). Analysis with the PDBePISA web server (Krissinel and Henrick, 2007), indicates this interface extends over a large surface of 910 Å^2, with individual contacts expected to only partially contribute to its stability. The PPP-mediated contacts between one Sec23 gelsolin-like domain and the neighbour Sec23 Zn-finger domain are part of this extended interface. As part of the extended lattice interface, Sar1 contacts the neighbouring Sec23 trunk domain. We detect a prominent contribution mediated by a 17-residue loop of Sec23 (residues 201-217, KPTGPGGAASHLPNAMN, which we name L-loop, for lattice) that is not visible in the X-ray structures. Secondary structure predictions denote this region as disordered and highly prone to protein binding

(Supplementary Fig. 7D). In our structure we can clearly visualise and model the L-loop in Sec23, which becomes partially ordered in its interaction with Sar1 (Fig. 6B). To assess the importance of the L-loop interaction in lattice formation and membrane tubulation, we mutated the 17 residues to a stretch of 5 glycine-serine repeats and tested this mutant in GUV budding reactions. The Sec23 L-loop mutant did not lead to any significant phenotype, with straight tubes forming (Fig. 6C). This is not unexpected, due to the loop's marginal contribution to the inner coat lattice interface. Indeed, weakening the lattice interface by mutating PPP motifs on Sec31 (Sec31-ΔPPP) does not change tube morphology either (Stancheva et al., 2020). However, when we aggravated the disruption by combining the Sec23 L-loop and Sec31-ΔPPP mutants, budding reactions showed a striking absence of straight tubules, and enrichment of multibudded profiles (Fig. 6D). This indicated that when inner coat interactions are significantly weakened, the outer coat becomes the main determinant of membrane remodelling and defaults to inducing spherical curvature. Indeed, when we also weakened outer coat vertex interactions

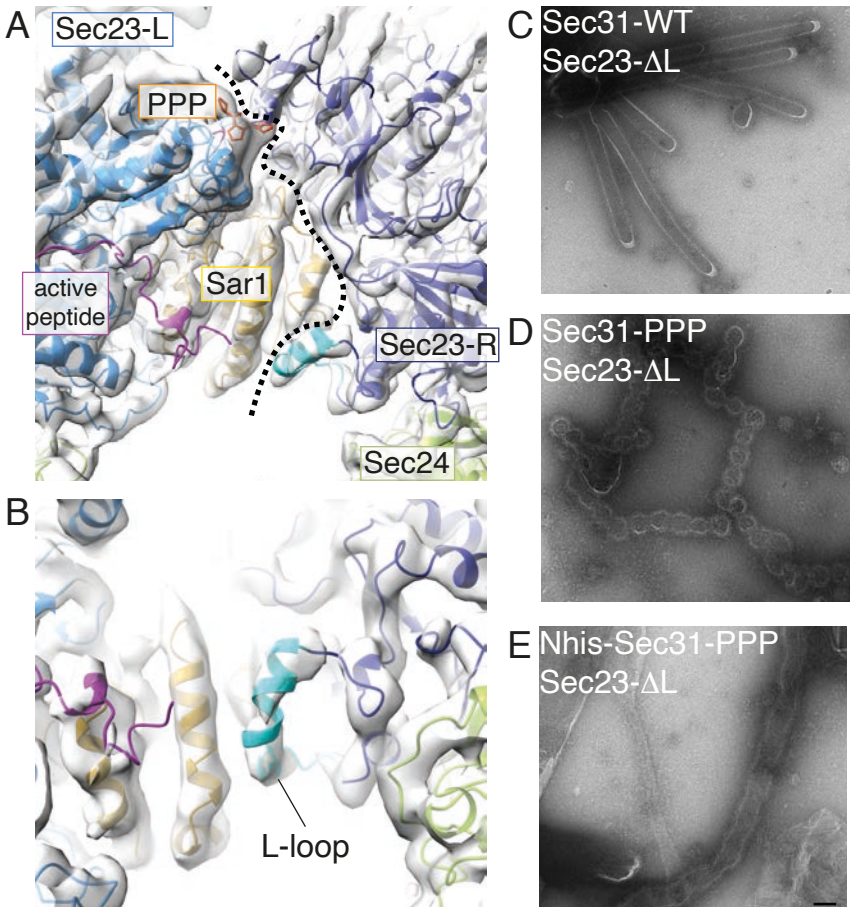

Figure 6. Interface between inner coat subunits

A. The interface between neighbouring inner coat subunits viewed from the top. A dotted line defines the boundary between two protomers.

B. Enlarged view of the Sec23-Sar1 interface, with the modelled Sec23 17-residue L-loop in dark cyan. This loop is disordered in the X-ray structure, but becomes ordered in the lattice, mediating interactions with Sar1.

C. GUV budding reconstitutions in the presence of wild type Sec31 and Sec23 lacking the L-loop show straight tubules, similar to wild type reactions.

D. Budding creates spherical profiles when Sec31 has all of its PPP sites mutated to alanine to further weaken inner coat assembly.

E. Floppy tubules form when, in addition to the conditions in D, Sec31 vertex interactions are destabilised with Nhis-Sec31. Scale bar 100 nm.

by using an N-terminal his-tagged version of Sec31-ΔPPP, budding gave rise to 'floppy' tubules rather than multibudded profiles (Fig. 6E).

Discussion

We have combined cryo-tomography with biochemical and genetic assays to obtain a complete picture of the assembled COPII coat at unprecedented resolution. We make a number of novel observations which allow us to piece together a picture of the COPII coat as a complex network of partially redundant interactions (Fig. 7). Structural and functional analysis of each interface reveals their role in coat assembly and membrane remodelling, shedding new light on the COPII-mediated membrane budding mechanism.

We map outer coat vertex interactions in detail, and dissect their role in membrane remodelling. Using an N-terminal deletion mutant of Sec31 in a range of assays that sample various degrees of membrane deformability, we show that outer coat assembly into cages is necessary *in vivo* to overcome membrane resistance to deformation, but is dispensable in conditions where membranes are more easily deformed thanks to the absence of certain cargo (Fig. 1 and Supplementary Fig. 3). Together with the previous report that outer coat cage stability is dispensable *in vitro* when inner coat turnover is inhibited (Hutchings et al., 2018), our results challenge the widely accepted role of the outer coat as a main driver of membrane curvature.

The interactions we observe between four Sec31 β-propeller subunits at the vertices of the outer coat lattice (Supplementary Fig. 3) are distinct from the analogous vertices seen in human Sec31 cages assembled *in vitro* in the absence of a membrane and Sar1 (Stagg et al., 2008, 2006). The vertex structure we report here for yeast proteins is much less compact, with deviations of over 15Å in the relative positions of neighbouring β-propellers. We saw this arrangement on spherical vesicles as well as empty cages, leading us to hypothesise that the vertex is more compact in humans than in yeast. It will be interesting to assess whether organisms with more complex secretory needs have selected tighter and more stable interactions at vertices.

Thorough structural analysis of the Sec13/31 rods reveals novel interactions between outer coat units. The elusive CTD of Sec31 forms a helical bundle, and its function was unknown to date. We show that Sec31 CTD is as an essential node of the outer coat network that binds to Sec31 α-solenoid domains (Fig. 2,3 and Supplementary Fig. 5). While we cannot assign a definite function to the Sec31 CTD, the fact that it is dispensable when membranes are made more deformable by depletion of certain classes of cargo is reminiscent of the role of Sec13 (Čopič et al., 2012), and of Sec31-ΔNTD, and suggests that Sec31 CTD contributes to coat rigidity and/or stability. One possibility is that CTD binding has a role in restricting the outer coat freedom to move once bound to the inner coat through its flexible disordered domain, thereby increasing the probability that outer coat lattice can form. Consistent with this, the outer coat on tubules reconstituted with Sec31-ΔCTD appears less ordered than in wild type conditions. Interestingly, human Sec31 proteins lacking the CTD assemble into cages (Paraan et al., 2018), indicating that either the vertex is more stable for human proteins, or that the CTD is important in the context of membrane budding but not for cage formation in high salt conditions. Our data paints a new picture of the assembled coat, where the outer coat C-terminal disordered region reaches down to bind and stabilise the inner coat, and then loops back to lock onto the outer coat lattice. Our data does not distinguish between a scenario in which C-terminal domains interact in *cis* or *trans* with outer coat rods, but it is interesting to hypothesise that trans-interactions might further stabilise the coat network (Fig. 7). While disruption of outer coat assembly at either Sec31 N-terminus or C-terminus is conducive to budding in conditions of high membrane deformability (for example budding GUVs), when both interactions are disrupted by using a Nhis-Sec31-ΔCTD construct, budding is inhibited, indicating that some level of outer coat assembly is required for membrane deformation.

We also discover a second, novel interaction within the outer coat: in addition to the known interaction of Sec31 β-propellers with each other at vertices, these domains can also bind to the Sec31 dimerisation

interface, at the centre of the α-solenoid region. This leads to extra outer coat rods creating a bridge between canonical rods (Fig. 4). Occasionally these extra rods form a canonical vertex interaction at one end, and an orthogonal interaction with other rods at the other end. Such rods 'glue' mismatched patches of outer coat lattice together: they might therefore be important for outer coat stabilisation in a context of flexibility and adaptability (Supplementary Fig. 6). It is interesting that we could only detect extra rods running in the left-handed direction, and connecting canonical right-handed rods. This could be explained by the scenario in which the Sec31 disordered PRD binds to multiple Sec23 subunits in tandem, leading to preferential orientation of the extra rods with respect to the inner coat. Due to limited particle numbers, the resolution we obtained does not allow us to precisely define the residues involved in the novel interaction between the β-propeller and the α-solenoid domains of Sec31. Higher resolution will be needed to inform mutational analysis and assess the physiological and functional relevance of this novel connection.

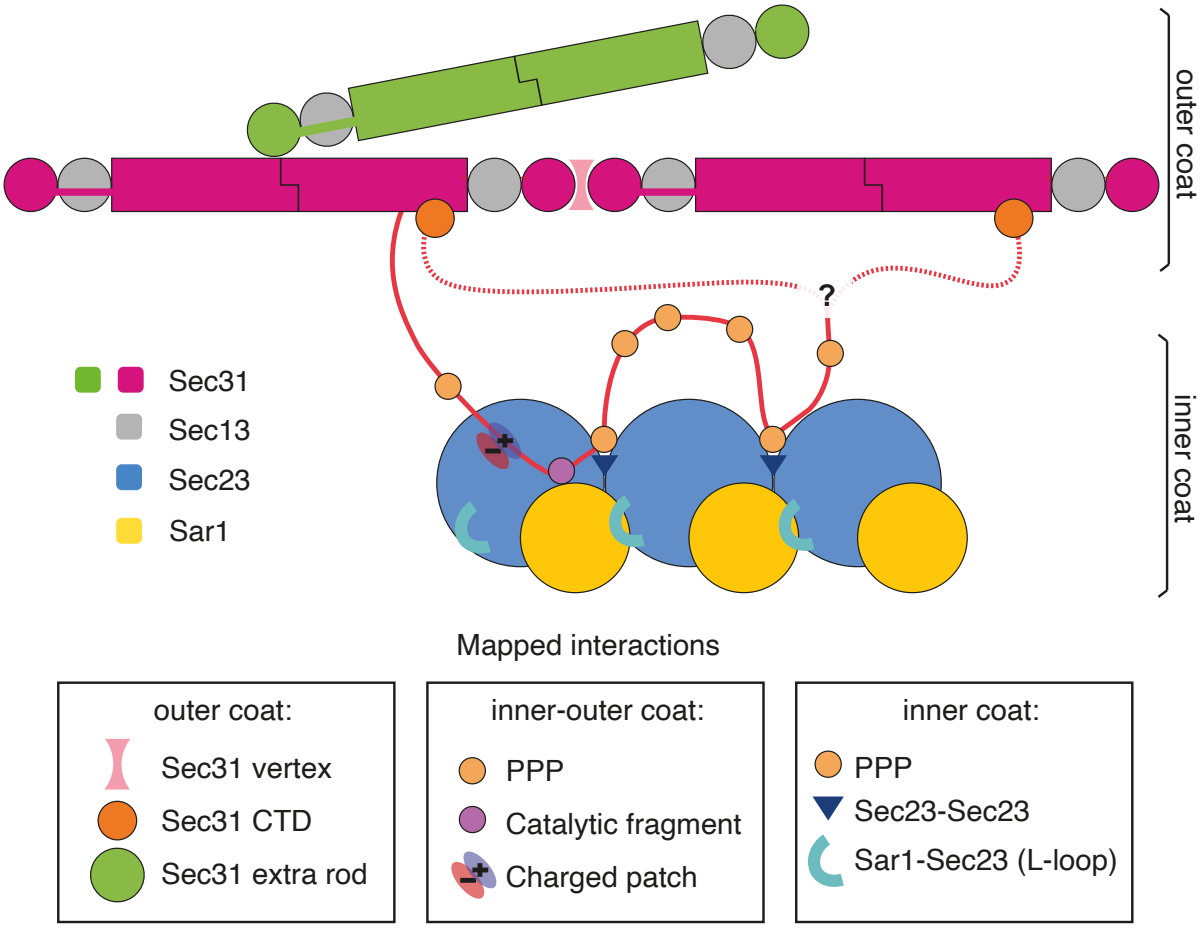

Figure 7. A map of the COPII coat assembly network

A model for how COPII assembles on membranes. Three sets of interactions contribute to coat assembly:

1. Outer-outer coat. Mediated by Sec31 β-propellers forming vertices, by Sec31 β-propellers binding to the α-solenoid domain of a different protomer to create 'bridging' rods, and by Sec31 CTD binding to Sec31 α-solenoid domain. It is unclear whether the latter interaction occurs in cis or trans.

2. Outer-inner coat. Mediated by Sec31 disordered region, contributing three interaction sites: triple proline motifs bind to Sec23 bridging between neighbouring subunits; the active peptide binds across Sec23 and Sar1 to accelerate GAP activity, and positively charged clusters bind to a negatively charged groove on Sec23.

3. Inner-inner coat. Mediated by Sec31 PPP motifs (see above), and by an extended lattice interface which includes Sec23-Sec23 interactions as well as Sec23-Sar1 interactions mediated by the L-loop.

Interactions between the outer and inner coat are mediated by Sec31 disordered PRD (Bi et al., 2007; Fath et al., 2007; Ma and Goldberg, 2016; Stancheva et al., 2020). By analysing the structure of the inner coat we confirm two interactions that have been previously defined and characterised structurally (Fig. 5): firstly, the Sec31 'active peptide' binds across Sec23 and Sar1, contributing residues in proximity to the GTP binding pocket, and accelerating Sec23 GAP activity (Bi et al., 2007). Secondly, Sec31 contains triple proline motifs, shared in metazoa by other COPII-interacting factors such as TANGO1 and cTAGE5 (Ma and Goldberg, 2016). These residues bind to the Sec23 gelsolin-like domain and appear to bridge adjacent inner coat subunits, aiding inner coat lattice formation (Hutchings et al., 2018; Ma and Goldberg, 2016). In addition, a novel, essential interaction between outer and inner coat layers was recently discovered. This is mediated by the negatively charged surface of Sec23 that was postulated to interact with positively charged clusters within the Sec31 PRD (Stancheva et al., 2020). We detect a prominent density bound to this region of Sec23, located within a groove formed at the junction between the gelsolin, helical and Zn-finger domains. We attribute this density to the interacting Sec31 positively charged regions (Fig. 5). Features of this extra density are less well-defined compared to the rest of the protein. Since multiple charge clusters in yeast Sec31 may contribute to this interaction interface (Stancheva et al., 2020), the low resolution could be explained by the fact that the density is an average of different sequences. Although we previously observed densities corresponding to the PPP and active peptide interactions in our structure assembled with Nhis-Sec31, the charged interaction was not detected (Hutchings et al., 2018). It is possible that ordering of the outer coat into a lattice improves the stability and occupancy of this interface.

Finally, interactions mediating inner coat assembly into a lattice are defined by our analysis. The first is the extended interface between Sec23 protomers that involves interaction with a neighbouring Sec23/Sar1 dimer and is bridged by Sec31 PPP motif (Fig. 6A). The second interface is a novel interaction between Sec23 and a neighbouring Sar1 molecule, mediated by a 17-residue loop (L-loop) in Sec23 which becomes ordered upon formation of the inner coat lattice (Fig. 6B), and whose importance in inner coat lattice assembly was confirmed biochemically.

Disrupting the inner coat lattice interface in combination with a Sec31 competent for outer coat assembly leads to budding of vesicles with spherical profiles, rather than a majority of straight tubules (Fig. 6D), indicating that outer coat assembly into cages dictates spherical membrane shape when the inner coat is unstable. This might be reflected in a physiological scenario where GTP-hydrolysis triggers inner coat turnover by removing Sar1 from the membrane, favouring spherical vesicles. Metazoan proteins such as TANGO1 and cTAGE5, which contain PPP motifs but do not accelerate GTP hydrolysis, could work by stabilising the inner coat interface while inhibiting GTP hydrolysis, favouring tubules and promoting transport of large carriers such as procollagen (Ma and Goldberg, 2016). Sec23 is a highly conserved protein, and is present in two paralogues in metazoa: Sec23A and B. While the two paralogues are thought to have largely redundant functions, mutations in Sec23A but not B cause defects in secretion of procollagen (Boyadjiev et al., 2006; Fromme et al., 2007). Human Sec23A and B are 85% identical, and the L-loop sequence is a region that varies significantly (Supplementary Fig. 7E). Because this region is important in stabilising lattice formation, we hypothesise it is involved in promoting formation of large carriers: the difference between Sec23A and B in the L-loop might confer an ability to differentially support large carrier budding, and explain their distinct roles in procollagen export disease.

We know from previous studies that partial disruption of both inner and outer coat layers is incompatible with life, but can be rescued by relieving the cell of bulky cargoes (Čopič et al., 2012; Stancheva et al., 2020). Here we show that weakened coat interactions at the level of both inner and outer coat leads to the formation of floppy tubules (Fig. 6E), suggesting the coat does partially assemble and impart some membrane deformation, but not sufficient for active cargo transport in cells. Together, these data suggest that a balance of lattice contacts between the inner and outer coats support membrane budding, and this balance can be tuned to achieve different morphologies depending on membrane deformability.

In summary, we have shown that COPII forms a complex network that assembles through partially redundant interactions, whose effects are combined for a productive budding event. We have obtained a detailed map of this network and have shown that the extent to which the presence and stability of each interaction are necessary depends on the membrane deformability. This makes the COPII system an ideal platform for regulation in response to dynamically changing cargo requirements, such as its abundance, shape and size.

Materials and methods

Cloning:

Yeast COPII components were cloned from the *Saccharomyces cerevisiae* S288c genome into appropriate expression vectors using In-Fusion (Takara), specifically: pETM-11 (AddGene) for Sar1 and pFASTBacHTb (AddGene) for Sec23/24 and Sec13/31. N-terminal hexa-histidine purification tags were cloned with an intervening TEV protease cleavage site for Sar1, Sec24 and Sec31.

Protein expression and purification:

Sar1

The pETM-11-Sar1 construct was transformed into BL21 using standard heat shock methods. Two litres of BL21 were induced with 1 mM IPTG for three hours at 25°C before harvesting. Sar1 was affinity purified following application to a 5 mL HisTrap column (GE Healthcare) equilibrated in lysis/binding buffer (50 mM Tris-HCl, 150 mM NaCl, 0.1% Tween-20 (v/v), 10 mM imidazole, 1 mM DTT, pH 8.0). Elution was achieved with a linear gradient of elution buffer (as for binding buffer, with 500 mM imidazole). Pure fractions were pooled and incubated with TEV protease at a 1:50 ratio of protease:Sar1 (w/w) in a sealed 10 kDa MWCO dialysis tube submerged in two litres of HisTrap binding buffer for overnight dialysis at 4°C. The dialysed product was reapplied to the HisTrap column with the flow-through collected and concentrated to ~0.7 mg/mL, determined using a Bradford assay.

Sec23/24

One litre of Sf9 insect cells (at $1x10^6$ cells/mL) were infected with baculovirus: 9 mL/L of untagged Sec23p and 3 mL/L of His-tagged Sec24p. These were incubated for three days at 27°C and 100 rpm shaking. Cells were harvested using a glass homogeniser and centrifuged at 167,424 g for one hour at 4°C. Sec23/24 was affinity purified following application to a 5 mL HisTrap column (GE Healthcare) equilibrated in lysis/binding buffer (20 mM HEPES (pH 8.0), 250 mM sorbitol, 500 mM potassium acetate, 10 mM imidazole, 10% glycerol and 1 mM DTT). Elution was achieved with a linear gradient of elution buffer (as for binding buffer, with 500 mM imidazole). Pure fractions were collected and diluted approximately two-fold with low salt anion-exchange binding buffer (20 mM Tris, 1 mM magnesium acetate, 0.1 mM EGTA, and 1 mM DTT, pH 7.5) before application to an equilibrated 5 mL HiTrap Q column (GE Healthcare). Elution was achieved with a linear gradient of elution buffer (as for binding buffer, with 1 M NaCl). Pure fractions were pooled and diluted to ~1.26 mg/mL with low salt buffer and 10% glycerol, which were then aliquoted, flash-frozen and stored at -80°C. The same protocol was applied for the Sec23 L-loop mutant. For Sec23-ΔL, residues 201-218 were mutated to 5xGS repeats using Sec23 pFastBacHTb as the template. The mutation was amplified by PCR and incorporated using InFusion. The same protein expression and purification protocol as WT Sec23/24 was used.

Sec13/31

One litre of Sf9 insect cells (at $1x10^6$ cells/mL) were infected with baculovirus: 9 mL/L of untagged Sec13p and 3 mL/L of His-tagged Sec31p. To obtain His-tagged Sec13/31 (Sec13/31-NHis), the same cell lysis and purification protocol (including buffers) was followed as for Sec23/24. Pure fractions from anion exchange were pooled and concentrated to approximately 2 mg/mL for 50 μL aliquots, which were flash-frozen and stored at -80°C.

For cleaved Sec13/31p an additional overnight TEV protease cleavage step was performed for His-tag removal prior to anion-exchange. Following the initial affinity purification with a 5 mL HisTrap column (GE Healthcare), the pooled eluate was incubated with TEV protease at a 1:50 ratio of protease:Sec13/31 (w/w) in a sealed 10 kDa MWCO dialysis tube submerged in two litres of HisTrap binding buffer for overnight dialysis at 4°C. The dialysed product was reapplied to the HisTrap column, the flow-through was collected, and then diluted approximately fourfold with low salt buffer for application to a 5 mL HiTrap Q column. Elution was achieved with a linear gradient of elution buffer (same as Sec23/24 Q elution buffer). Pure fractions were pooled and concentrated to approximately 2 mg/mL for 50 μL aliquots, which were flash-frozen and stored at -80°C.

On the day of GUV BR preparation, Sec13/31 and/or NHis-Sec13/31 aliquots were thawed and gel-filtrated on a 2.4 mL Superdex200 column (GE Healthcare) mounted on a ÄktaMicro (GE Healthcare) system, equilibrated in HKM buffer (20 mM HEPES, 50 mM KOAc and 1.2 mM MgCl2, pH 6.8). Cleaved and uncleaved versions of the Sec13/31 mutants used in this study were prepared in the same as the wild-type protocol detailed above.

For the Sec13/31-ΔNTD, a C-terminally His-tagged version of Sec31 truncated at position 373 was used. This was derived from the Sec31-NHis pFASTBacHTb construct using InFusion cloning. For the Sec13/31-ΔCTD, a N-terminally His-tagged version of Sec31 covering residues 1-1114 was used. This was derived from the Sec31-NHis pFASTBacHTb construct using InFusion cloning. For Sec13/31-ΔPPP, a synthetic DNA construct with seven PPP to SGS mutants (853-855, 965-967, 966-968, 981-983, 1042-1044, 1096-1098 and 1107-1109) was inserted into the Sec31-NHis pFASTBacHTb construct using InFusion.

GUV budding reactions:

Giant unilamellar vesicles (GUVs) were prepared by electroformation (Angelova and Dimitrov, 1986) from 10 mg/mL of the "major-minor" lipid mixture (Ken Matsuoka et al., 1998) suspended in a 2:1 chloroform:methanol solvent mix, as described previously (Hutchings et al., 2018). The mixture is spread over two Indium Tin Oxide (ITO)-coated glass slides, which are sandwiched with a silicon spacer to create a chamber that is then filled with 300 mM sucrose. An alternating voltage of 10 Hz and 3 V (rms) was applied for 6-8 hours using copper tape attached to the ITO-coated slides. GUVs were harvested by gentle aspiration from the chamber and applied to 500 μL of 300 mM glucose for gravity sedimentation overnight at 4°C. The supernatant was carefully aspirated and discarded to leave a ~30-50 μL GUV pellet the next day. GUVs were used within two days of harvesting.

For GUV budding reactions (BRs), COPII proteins were incubated at defined concentrations (1 μM Sar1p, 320 nM Sec23/24p, 173 nM Sec13/31p) with 1 mM GMP-PMP (Sigma-Aldrich), 2.5 mM EDTA (pH 8.0) and 10% GUVs (v/v). The same concentrations were used for BRs with mutant COPII components. Reactions were left at room temperature for 1-3 hours prior to negative stain or vitrification.

Yeast strains and plasmids:

Yeast strains and plasmids used in this study were all generated using standard molecular biology techniques. The yeast strains used were previously published: LMY1249 (*sec31::NAT pep4::TRP ade2-1 his3-11 leu2-3,112 + [pYCp50::SEC31-URA3])* described (Hutchings et al., 2018) and VSY015 (*sec31::NAT emp24::KANMX pep4::TRP ade2-1 his3-11 leu2-3,112 + [pYCp50::SEC31-URA3])* described (Stancheva et al., 2020). Plasmids were introduced into yeast using standard LiAc transformation methods. Cultures were grown at 30°C in standard rich medium (YPD: 1% yeast extract, 2% peptone, and 2% glucose) or synthetic complete medium (SC: 0.67% yeast nitrogen base and 2% glucose supplemented with amino acids) as required. For testing viability, strains were grown to saturation in SC medium selecting for the mutant plasmid overnight at 30°C. 10-fold serial dilutions were made in 96 well trays before spotting onto 5FOA plates (1.675% yeast nitrogen base, 0.08% CSM, 2% glucose, 2% agar, 0.1% 5-fluoroorotic acid). Plates were scanned at day 2 or day 3 after spotting and growth at 30°C. The *SEC31* WT plasmid used in this study (VSB49) was described (Stancheva et al., 2020) and consists of *SEC31* PCR-amplified with native 500 bp upstream and downstream of the gene and cloned in BamHI/NotI sites of pRS313

(*HIS, CEN*; (Sikorski and Hieter, 1989)). Truncations were introduced by site-directed mutagenesis using the QuikChange system (Agilent) and Gibson Assembly (New England Biolabs) as per manufacturers' instructions to generate VSB146 (stop codon at position 1114) and VSB131 (deletion of Val2-Gln372). All experiments were repeated three times and a representative is shown.

Liposome binding:

Liposome binding experiments were performed as described (Miller et al., 2002). Briefly, synthetic liposomes of "major/minor" composition (50 mol% phosphatidylcholine, 21 mol% phosphatidylethanolamine, 8 mol% phosphatidylerine, 5 mol% phosphatidic acid, 9 mol% phosphatidylinositol, 2.2 mol% phosphatidylinositol-4-phosphate, 0.8% mol% phosphatidylinositol-4,5-bisphosphate, 2 mol% cytidine-diphosphate-diacylglycerol, supplemented with 2 mol% TexasRed-phosphatidylethanolamine and 20% (w/w) ergosterol) were dried to a lipid film in a rotary evaporator and rehydrated in HKM buffer (20mM HEPES pH 7.0, 160mM KOAc, 1mM $MgCl_2$). The lipid suspension was extruded 17 times through a polycarbonate filter of 0.4 µm pore size. Purified COPII components and lipids were mixed to final concentrations of 0.27mM liposomes, 15µg/ml Sar1, 20µg/ml Sec23/Sec24, 30µg/ml Sec13/Sec31 and 0.1mM nucleotide in 75µl HKM Buffer. Binding reactions were incubated for 30 min at 25°C. Each sample was mixed with 50µl 2.5M Sucrose-HKM, then 100µL transferred to an ultracentrifuge tube, overlaid with 100µl 0.75M Sucrose-HKM and 20µl HKM. The gradients were spun (100 000 rpm, 25 min, 24°C with slow acceleration/deceleration) in a Beckman TLA-100 rotor. The top 30µl of the gradients were collected and normalised for lipid recovery using Typhoon FLA 7000 scanner (GE). Samples were then resolved by SDS-PAGE and visualised using SYPRO Red staining. All experiments were repeated three times and a representative is shown.

Microsome budding assays:

Microsomal membranes were prepared from yeast as described (Wuestehube and Schekman, 1992). Briefly, yeast cells were grown to mid-log phase in YPD (1% yeast extract, 2% peptone, and 2% glucose), harvested and resuspended in 100mM Tris pH 9.4/10mM DTT to 40 OD_{600}/ml, then incubated at room temperature for 10 min. Cells were collected by centrifugation and resuspended to 40 OD_{600}/ml in lyticase buffer (0.7M sorbitol, 0.75X YPD, 10mM Tris pH 7.4, 1mM DTT + lyticase 2µL/OD_{600}), then incubated at 30ºC for 30 min with gentle agitation. Cells were collected by centrifugation, washed once with 2X JR buffer (0.4M sorbitol, 100mM KOAc, 4mM EDTA, 40mM HEPES pH 7.4) at 100 OD_{600}/ml, then resuspended in 2X JR buffer at 400 OD_{600}/ml prior to freezing at -80ºC. Spheroplasts were thawed on ice, and an equal volume of ice cold dH20 added prior to disruption with a motor-driven Potter Elvehjem homogenizer at 4ºC. The homogenate was cleared by low speed centrifugation and crude membranes collected by centrifugation of the low-speed supernatant at 27,000 x g. The membrane pellet was resuspended in ~6mL of buffer B88 (20mM HEPES pH 6.8, 250mM sorbitol, 150mM KOAc, 5mM $Mg(OAc)_2$) and loaded onto a step sucrose gradient composed of 1mL 1.5M sucrose in B88 and 1mL 1.2M sucrose in B88. Gradients were subjected to ultracentrifugation at 190,000 x g for 1h at 4ºC. Microsomal membranes were collected from the 1.2M/1.5M sucrose interface, diluted 10-fold in B88 and collected by centrifugation at 27,000 x g. The microsomal pellet was resuspended in a small volume of B88 and aliquoted in 1mg total protein aliquots until use.

Budding reactions were performed as described (Miller et al., 2002). Briefly, 1mg of microsomal membranes per 6-8 reactions was washed 3x with 2.5 M urea in B88 and 3x with B88. Budding reactions were set up in B88 to a final volume of 250 µl at the following concentrations: 10µg/µl Sar1, 10µg/µl Sec23/Sec24, 20µg/µl Sec13/Sec31 and 0.1mM nucleotide. Where appropriate, an ATP regeneration mix was included (final concentration 1mM ATP, 50µM GDP-mannose, 40mM creatine phosphate, 200µg/ml creatine phosphokinase). Reactions were incubated for 30 min at 25°C and a 12 µl aliquot collected as the total fraction. The vesicle-containing supernatant was collected after pelleting the donor membrane (15 000 rpm, 2 min, 4°C). Vesicle fractions were then collected by centrifugation in a Beckman TLA-55 rotor (50 000 rpm, 25 min, 4°C). The supernatant was aspirated, the pelleted vesicles resuspended in SDS sample buffer and heated for 10 min at 55°C with mixing. The samples were then

561 analysed by SDS-PAGE and immunoblotting for Sec22 (Miller lab antibody) and Erv46 (a gift from
562 Charles Barlowe). All experiments were repeated three times and a representative is shown.

563 *EM sample preparation:*

564 For cryo-electron tomography:

565 4 μL of the GUV COPII BR was applied to negatively glow-discharged C-flat holey carbon coated gold
566 grids (CF-4/1-4AU, Electron Microscopy Sciences), blotted from both sides (60 seconds pre-blot wait,
567 blot force setting five, and four second blot time) and plunge-frozen in 100% liquid ethane on a Vitrobot
568 Mark IV (FEI) set to 4°C and 100% humidity. 3 μL of BSA-blocked 5 nm gold nanoparticles (BBI Solutions)
569 were added to a 30 μL GUV BR and gently agitated just prior to vitrification. Vitrified grids were stored
570 in liquid nitrogen dewars to await data collection.

571 For negative stain:

572 4 μL of the GUV COPII BR was applied to negatively glow-discharged grids (Carbon film 300 Copper
573 mesh, CF300-Cu), stained with 2% uranyl acetate, blotted with filter paper and air-dried at room
574 temperature. Grids were imaged using either a Tecnai 120 keV TEM (T12) fitted with a CCD camera, or
575 a Tecnai 200 keV TEM (F20) fitted with a DE20 detector (Direct Electron, San Diego). Unaligned and
576 summed frames were collected for F20 images with a dose of 20-30 e^-/pixel/second.

577 *Cryo-electron tomography data collection:*

578 For wild-type COPII GUV BRs, a total of 286 dose-symmetric tilt series (Hagen et al., 2017) with +/- 60°
579 tilt range and 3° increments were acquired on Titan Krios operated at 300 keV in EFTEM mode with a
580 Gatan Quantum energy filter (20 eV slit width) and K2 Summit direct electron detector (Gatan,
581 Pleasanton CA) at ~1.33 Å/pixel. Data were collected at the ISMB EM facility in Birkbeck College and at
582 the Cryo-EM Service Platform at EMBL Heidelberg. For ΔCTD-Sec31, 47 dose-symmetric tilt series were
583 collected at Birkbeck with a K3 direct detector (Gatan, Pleasanton CA) at ~ 1.38 Å/pixel. For all sessions,
584 defocus was systematically varied between 1.5 and 4.5 μm (Table 1). Data was collected automatically
585 using SerialEM (Mastronarde, 2005) after manually selecting tubes using the AnchorMap procedure.
586 Dose per tilt varied between 2.9 and 3.7 $e^-/Å^2$, equating to ~120 and ~150 $e^-/Å^2$ in total respectively,
587 depending on the dataset (Table 1).

588 *Cryo-tomography data processing:*

589 Tilt frames from Birkbeck were aligned using whole frame alignment with MotionCor2 (Zheng et al.,
590 2017), which were amalgamated into ordered stacks. Tilt series were either aligned manually with
591 IMOD or automatically with the Dynamo tilt series alignment (*dtsa*) pipeline (Castaño-Díez et al., 2012).
592 Weighted back-projection (WBP) was used to reconstruct bin8x tomograms with 50 iterations of SIRT-
593 like filtering for initial particle-picking and STA. CTF estimation was performed with CTFFIND4 on a
594 central rectangular region of the aligned and unbinned tilt series, as done previously (Hutchings et al.,
595 2018). The uncropped, aligned and unbinned tilt series were dose-weighted using critical exposure
596 values determined previously using custom MATLAB scripts (Grant and Grigorieff, 2015). 3D-CTF
597 correction and tomogram reconstruction was performed using the novaCTF pipeline (Turoňová et al.,
598 2017), with bin2x, bin4x and bin8x versions calculated using IMOD *binvol* (Kremer et al., 1996).

599 *Subtomogram averaging:*

600 All STA and subsequent analysis was performed using a combination of Dynamo (Castaño-Díez et al.,
601 2012) and custom MATLAB scripts.

602 Inner coat:

603 Initial particle-picking for the inner coat was performed using previously established protocols
604 (Hutchings et al., 2018; Zanetti et al., 2013). Briefly, tube axes were manually traced in IMOD to
605 generate an oversampled lattice of cylindrical surface positions with angles assigned normal to the

surface. 32^3 voxel boxes were extracted from bin8x SIRT-like filtered tomograms for one round of initial reference-based alignments using a resampled and 50 Å low-pass filtered version of the inner coat reconstruction EMDB-0044 (Hutchings et al., 2018). Manual inspection of geometric markers using the UCSF Chimera placeObjects plug-in (Pettersen et al., 2004; Qu et al., 2018) confirmed convergence of oversampled coordinates onto the pseudo-helical inner coat lattice.

To rid outliers from the initial alignments, three strategies were used. Firstly, distance-based cleaning was applied using the Dynamo "separation in tomogram" parameter, set to four pixels. This avoids duplication of data points by identifying clusters of converged particles and selecting the one with the highest cross-correlation (CC) score. Secondly, particles were cleaned based on their matching lattice directionality. Initial alignments were conducted on a tube-by-tube basis using the Dynamo in-plane flip setting to search in-plane rotation angles 180° apart. This allowed to assign directionality to each tube, and particles that were not conforming to it were discarded by using the Dynamo *dtgrep_direction* command in custom MATLAB scripts. Thirdly, manual CC-based thresholding was implemented to discard misaligned particles. As seen previously (Hutchings et al., 2018), particles on the tubule surface exhibited an orientation-dependent (Euler angle θ) CC score whereby top and bottom views had lower CC values. These were reweighted using the same polynomial fit for θ versus CC (MATLAB fit with option 'poly2') as described previously for more convenient thresholding. The cleaned initial coordinates were then combined and divided into half datasets for independent processing thereon.

Subsequent STA progressed through successive binning scales of 3DCTF-corrected tomograms, from bin8x to 4x, 2x then unbinned. At each level, angular and translational searches were reduced, with the low-pass filter determined by the Fourier shell correlation (FSC) 0.5 cut-off between the two half-maps. A saddle-shaped mask mimicking the curvature of the membrane at the height of the inner coat layer was used throughout. A total of 151,176 particles contributed to the map.

Half maps were used for density modification using Phenix (Terwilliger et al., 2020). The same mask used for alignments was imposed, and the density modification procedure was carried out without reducing the box size. All other parameters were used as default. After density modification, the map was further sharpened using the 'autosharpen' option in Phenix (Liebschner et al., 2019).

Outer coat:

To target the sparser outer coat lattice for STA, we used the refined coordinates of the inner coat to locate the outer coat tetrameric vertices. Oversampled coordinates for the outer coat were obtained by radially shifting refined inner coat coordinates by eight pixels further away from the membrane, following initial alignments from SIRT-like filtered tomograms (Supplementary Fig. 1B). 64^3 voxel boxes were extracted from bin8x SIRT-like filtered tomograms for one round of initial reference-based alignments using a resampled and 50 Å low-pass filtered version of the outer coat tetrameric vertex reconstruction EMDB-2429 (Zanetti et al., 2013). Again, manual inspection of positions and orientations with the placeObject plug-in confirmed conformity to the expected lozenge-shaped outer coat lattice (Supplementary Fig. 1). Moreover, density for the neighbouring outer coat vertices emerged outside of the alignment mask and template, suggesting these initial alignments are not suffering from reference bias. The cleaned initial coordinates were then combined and divided into half datasets for independent processing thereon. The rhomboidal lattice can be appreciated by plotting the frequency of neighbouring particles for each vertex in the STA dataset (Supplementary Fig. 1D, left panel). Analysis of the relative positions between the inner coat and outer vertex did not reveal any defined spatial relationship (Supplementary Fig. 1D, right panel).

Subsequent STA progressed through successive binning scales of 3DCTF-corrected tomograms, from bin8x to 4x, to 2x, for a final pixel size of 2.654 Å. At each level, angular and translational searches were reduced, with the low-pass filter determined by the Fourier shell correlation (FSC) 0.5 cut-off between the two half-maps. A mask mimicking the curvature of the outer coat layer was used throughout. Prior to sharpening of the final unbinned map using relion 'postprocessing', the final half dataset averages were amplitude-weighted according to the sum of the combined CTFs.

The refined positions of vertices were used to extract two distinct datasets of left and right-handed rods respectively using the dynamo sub-boxing feature. Left-handed rods were processed as vertices, except that a cylindrical mask was used during alignments. Right handed rods were subjected to classification in dynamo using multi-reference alignments. One class contained canonical rods, and particles belonging to this class were further processed as above. Two classes which contained the extra rod attachment were combined after applying a 180° in-plane rotation to particles in one class. After that, processing was carried out as for the other subtomograms.

The number of particles that contributed to outer coat averages is reported in Table 1.

Sec31-ΔCTD outer coat rods:

Oversampled coordinates for the outer coat were obtained in the same way as the WT dataset. Initial alignments using the previously resolved tetrameric vertex (EMDB-2429) did not produce lattice patterns conforming to the expected lozenge-shape as judged from the placeObjects inspection. This was confirmed by the subtomogram neighbour analysis for the refined initial alignment coordinates. Furthermore, the resulting average did not reveal new features emerging outside of the mask or initial reference. To confirm that Sec31-ΔCTD rods lack the appendage seen in the WT rod maps, we instead performed initial alignments against a rod without handedness. For this, the final left-handed rod from the WT dataset was taken and rigid body fitted with the crystal structure (PDB 4bzk) in UCSF Chimera (Pettersen et al., 2004) to generate a 30 Å *molmap*. This was duplicated, mirror-symmetrised with the flipZ command in Chimera, and rotated along the axis of the rod by 180°, and summed with the original molmap using *vopMaximum* to create a Sec13/31 rod without handedness. This was used as a template for initial alignments, keeping Dynamo parameters consistent with vertex alignments at the same stage. This resulted in a rod which regained the original handedness of Sec13/31, suggesting no reference bias. To clean the dataset of misaligned particles, MRA with five classes and no shifts or rotations allowed was performed for 100 iterations. Two stable classes comprising ~90% of the data emerged as recognisable Sec13/31 rods. Refinement of each of these selected classes against a wild type left-handed rod gave averages that lacked the putative CTD appendage.

The procedure was repeated independently for two half datasets for resolution assessment.

Subtomogram neighbour analysis:

To provide a semi-quantitative readout for the degree of lattice order, neighbour plots were calculated and used in a similar way to previous STA studies (Kovtun et al., 2020, 2018). Briefly, all neighbouring particles are identified within a user-defined distance on a particle-by-particle basis. The relative orientation and distance to the matched particle is used to fill the relevant pixel in a master volume relative to its centre, which accumulates into a volume of integers. The final volumes are divided by the number of searched particles and normalised to a maximum intensity of one. For convenient visualisation, pixels in Z were summed to create heatmap representations (Supplementary Fig 1D). This heatmap reflects the frequency of neighbouring particles and in a well-ordered lattice, peaks are visible. Furthermore, this master volume retains matched particle pairings, and can be masked to select specific relationships in the dataset (Supplementary Fig. 6C).

Outer coat in spherical vesicles and cages:

Vesicles and cages were identified, and vertices manually picked from gaussian filtered binned x8 volumes using UCSF Chimera (Pettersen et al., 2004). Initial orientations were assigned normal to the vesicle or cage centre, and the in-plane rotation angle was randomised. Vertices were then aligned for one iteration to the relevant starting reference (Supplementary Fig. 4), searching out of plane angles within a cone and the full in plane rotation range.

Fitting and interpretation:

The map output from phenix.resolve_cryoem (Terwilliger et al., 2020) and the further sharpened map were used to provide guidance for model building.

Crystal structures of Sec23 (2QTV), Sec24 (1PCX), Sar1 (2QTV), Tango1 (5KYW) and Sec31 active peptide (2QTV) were fitted to the reconstruction using UCSF Chimera (Pettersen et al., 2004) and Coot (Emsley et al., 2010).

Two copies of each protein were placed, representing two protomeric assemblies. Clashes between Sec23 from adjacent protomers were resolved by manual rebuilding. Clear density was also observed for residues 201-217 of Sec23, 363-371and 463-466 of Sec24, and 157-159 of Sar1, and were manually built as they were absent from the crystal structures.

The model was refined with phenix.real_space_refine against the sharpened map, and validated with phenix.validation_cryoem (dev 3885) (Table 3).

Homology modelling:

Sec31 residues 481-1273 (encompassing PRD and CTD regions) was used to search for remote homologues using the HHpred server (Zimmermann et al., 2018), and identifying SRA1 as the closest homologue in the PDB database (PDB 2MGX, E-value 2.3E-15). To confirm the homology, the Sec31 protein sequence (Uniprot id: P38968) was used to search the CATH database of functional families (Sillitoe et al., 2015), generating a significant hit to a Sec31 CTD functional family (E-value 6.0E-48). SRA1 matched this family with an E-value of 0.0001, which is within the threshold for homology modelling using functional family matches, based on previous benchmarks (Lam et al., 2017).

Homology models of Sec31 CTD were built using a combination of HHpred and Modeller (Webb and Sali, 2017), based on the highest-ranking homologue structure of SRA1 (Bilinovich et al., 2014). According to calculations from proSA web-server (Wiederstein and Sippl, 2007), the model has a z-score of -6.07, similar to that of the template (-5.38), and in line with that of all experimentally determined structures.

726 *Tables:*

727 Table 1: Data collection parameters

	WT COPII (1)	WT COPII (2)	ΔCTD
Grids	C-flat holey carbon coated gold grids (CF-4/1-4AU, Electron Microscopy Sciences)	C-flat holey carbon coated gold grids (CF-4/1-4AU, Electron Microscopy Sciences)	Lacey Carbon film, 200 Copper, (S166-3, Agar Scientific)
Cryo-specimen freezing	Vitrobot Mark IV	Vitrobot Mark IV	Leica EM GP
Electron microscope	Titan Krios, EMBL	Titan Krios, Birkbeck	Titan Krios, Birkbeck
Detector	K2 direct detector, Gatan	K2 direct detector, Gatan	K3 direct detector, Gatan
Datasets	1	1	1
Micrographs (used in processing)	137 tomograms	149 tomograms	47 tomograms
Voltage (keV)	300		
GIF energy filter slit width (eV)	20		
Electron exposure ($e^-/Å^2$)	~ 120	~ 150	~ 120
Sampling interval	1.33 Å/pixel	1.327 Å/pixel	0.69 Å/pixel (superresolution), 1.38 Å/pixel 2x2 binned.
Exposure time	0.25 sec frame / 0.75 sec total	0.1 sec frame / 1 sec total	0.08 sec frame / 0.4 sec total
Defocus range	-1.5 to -4.5 µm	-1.5 to -4.5 µm	-1.5 to -3.5 µm
Defocus determination	CTFFIND4		

728

729 Table 2: 3D STA reconstructions and model refinement

	Inner coat	Outer coat			
		Vertex	Left-handed rod	Right-handed rod	Right-handed rod with extra
Particle box size	196	128	128	128	128
Number of particles used	151,176	14,099	16455	7958	7195
Initial map generation	Dynamo	Dynamo	Dynamo	Dynamo	Dynamo
Map refinement	Dynamo	Dynamo	Dynamo	Dynamo	Dynamo
Resolution	4.6 Å	12 Å	11 Å	13 Å	15 Å

Table3: refinement statistics for the inner coat

Model composition	
Protein residues	3413
No. Ligands	8
Protein atoms	26852
Ligand atoms	70
Model Resolution @ FSC 0.5 (Å)	4.7
Map CC (mask)	0.716
Average B-factor (all atoms) (Å^2)	158.4
RMS deviations – Bonds (Å)	0.01
RMS deviations – Angles (deg)	1.52
Molprobity Score	2.18
Clashscore	13.11
Ramachandran plot (%)	
Favoured	89.7
Allowed	10.1
Outlier	0.21
C-beta deviations (%)	0.00
Rotamer Outliers (%)	0.07

Supplementary Figure LEgends

Supplementary Figure 1. Overview of subtomogram averaging.

A. A typical view of GUV budding on grids. Scale bar 1um.

B. Workflow for extraction of outer coat subtomograms. Top: aligned inner coat subunits arrange in a lattice. Middle: radially shifted coordinates from inner coat lattice points are used to extract outer coat particles. This oversamples the outer coat lattice. Bottom: alignments of outer coat particles with large shift in their xy plane but restricted shifts in the z direction leads to finding outer coat subunit accurately, as shown by the outer coat lattice pattern. This strategy was necessary to avoid the high-signal inner coat to bias the alignments.

C. Left panel: the starting reference is shown overlaid with the mask used. Right panel: the average obtained after one iteration clearly shows continuous density outside the mask, including neighbouring vertices and underlying smeared inner coat layer, indicative of genuine alignments.

D. Left panel: plot of the positions of neighbouring vertices to each aligned vertex shows the expected pattern. Right panel: plot of neighbouring inner coat subunits with respect to each vertex does not show any pattern, indicating the two coat layers are disordered with respect to each other. Scale bar 50 nm.

Supplementary Figure 2. Resolution of subtomogram averages.

A. Fourier Shell Correlation between independently processed half maps for the outer coat structures, colours as indicated in the legend. Line indicating FSC=0.143 is drawn.

B. Fourier Shell Correlation between independently processed half maps for the inner coat.

Supplementary Figure 3. Vertex interaction between Sec31 N-terminal β-propellers.

A. A bottom view of the vertex reconstruction (outlined transparent white), with fitted models (Sec31 in dark red and orange, and Sec13 in grey). In the model, the N-terminal residues are highlighted in blue, and the stubs of an acidic loop missing from the X-ray structures are highlighted in green. The difference map between the subtomogram average and the model is shown in green, and is consistent with being occupied by the acidic loop.

B. *In vitro* budding experiments using yeast microsomal membranes incubated with Sar1, Sec23/Sec24, Sec13 with the indicated mutant of Sec31, and the indicated nucleotides. Vesicle release from the donor membrane is measured by detecting incorporation of COPII cargo proteins, Sec22 and Erv46, into a slowly sedimenting vesicle fraction. When the NTD of Sec31 is missing, no budding is detected.

C. Flotation assays measure recruitment of COPII proteins to buoyant liposomes. Sec31-ΔNTD is recruited with similar efficiency to wild type Sec31, indicating that the budding and viability defects are not due to low recruitment levels.

D. Negatively stained GUV budding reconstitutions with Sec31 deleted of its N-terminal β-propeller domain show

tubulation and ordered inner coat lattice. Scale bar 100 nm.

E. Anti-Sec31 Western Blot of the 5-FOA derived SEC31 and sec31-ΔNTD strains showing that the expected size of Sec31 variants is present in the surviving cells.

F. Comparison of the vertex reconstructed from coated membrane tubules (this study), with that of cages obtained in the absence of membranes (Noble et al., 2013). The '-' protomers are in dark red, and the '+' protomers are shown in orange and blue respectively.

G. The fitted atomic models were superimposed on a '-' Sec31 protomer, and the relative positions of the neighbouring '+' protomers are overlapped, highlighting the differences between the two architectures.

Supplementary Figure 4. Vertices on round vesicles and empty cages are hollow.

A. 79 vertices were manually picked from spherical vesicles, and aligned against starting references originated either from a low-pass filtered version of the vertex obtained from tubules, or to the vertex of soluble cages obtained through in vitro assembly in the absence of membranes. In both cases, averages show a hollow architecture, more similar to the vertex arrangement we see on membrane tubules. Places vertex confirm the alignments are correct.

B. As in A, but 205 vertices were manually picked from membrane-less cages that were found in the cryo-tomograms as by-products of budding reactions. Scale bar 50 nm.

Supplementary Figure 5. Sec31 CTD characterisation.

A. Secondary structure predictions of Sec31 CTD indicate the presence of a folded domain, consisting mainly of α-helices.

B. A homology model for the Sec31 CTD was built based on SRA1, a mammalian homologue. The homology model was fitted to the appendage density and shows consistency of features.

C. Side by side comparison of the homology model of the CTD with the SRA1 template used.

D. As in Supplementary Fig. 4C. When Sec31 CTD is missing, weak budding is detected with non-hydrolysable GTP analogues but not with GTP.

E. As in Supplementary Fig. 4E. Sec31-ΔCTD is efficiently recruited to membranes, indicating the functional defects are not a consequence of low recruitment levels.

Supplementary Figure 6. Analysis of extra rods connecting between right-handed rods.

A. Right handed rods after the first round of alignments (bin x 8) showed prominent extra density.

B. After classification, a class emerged of right-handed rods which had a structured domain attached to the dimerization interface, resembling a tandem of β-propeller domains of Sec13-31 rods. Sub-boxing was performed by extracting particles at the predicted centre of the extra rods, and subtomogram averaging and subsequent alignments clearly converged into a Sec13-31 rod structure.

C. The plotted position of vertices neighbouring the extra rods. Given the extra rods position within the outer coat lattice (green line), vertices are predicted to position at the corners of a rhombus (dotted pink lines). An extra peak was detected in the neighbour plot, which corresponds to the tip of the extra rod (red circle).

D. Selecting and averaging extra rod particles based on masks on the neighbour plot clearly shows that some of these rods are connected to a right-handed rod on one side, and a vertex on the other.

E. Rods selected in D (green) were placed together with the canonical rods and vertices (dark pink and red, respectively), showing that they bridge between patches of mismatched outer coat lattice.

Supplementary Figure 7. Inner coat subtomogram averaging.

A. Overview of the sharpened map, with the central subunit coloured according to the model.

B. The X-ray-based model of Sec23, Sec24 and Sar1 was refined in the map, as detailed in the methods.

C. A close up view of the model in the core of Sar1, showing clear separation of β-strands and density for the bound nucleotide.

D. Disorder prediction of the Sec23 region around the L-loop (inset), as done with the PSIPRED server (Buchan and Jones, 2019; Jones and Cozzetto, 2015).

E. Alignment between human Sec23A and B paralogues shows very high conservation throughout the proteins, aside of a short region corresponding to the L-loop.

Acknowledgements

We thank Euan Pyle and Natasha Lukoyanova for comments on the manuscript. We thank Natasha Lukoyanova at the ISMB Birkbeck cryo-EM lab, and Wim Hagen at the EMBL cryo-EM facility in Heidelberg for cryo-tomography data collection, Tom Terwilliger at Los Alamos National Laboratory for advice on density modification procedures, and Christine Orengo and Natalie Dawson for help with Sec31 CTD bioinformatics analysis. **Funding**: This work was supported by grants from the Academy of Medical Sciences (Springboard award SBF0031030), the ERC (StG 852915 – CRYTOCOP) and the BBSRC (BB/T002670/1) to GZ, the UK Medical Research Council (MRC_UP_1201/10) to EAM and the Wellcome Trust (102535/Z/13/Z) to ACMC. Cryo-EM data for this investigation were collected at Birkbeck College, University of London, with financial support from the Wellcome Trust (202679/Z/16/Z and 206166/Z/17/Z), and at the Cryo-EM Service Platform at EMBL Heidelberg.

Author contributions: Conceptualization: GZ, JH; Funding acquisition: GZ, EAM; **Investigation**: Sample preparation: JH, NRB; cryo-tomography data collection: JH; cryo-tomography and subtomogram averaging data processing: JH, GZ; yeast viability and microsome budding assays: VS, EAM; model building and refinement: AC. **Writing**: original draft: GZ, JH; review and editing: all authors. **Data and materials availability**: We have deposited the EM maps and models to the Electron Microscopy and Protein Data Banks with accession codes: EMD-11193,11194,11197,11198,11199,11264 and PDB 6ZG5,6ZG6,6ZGA,6ZL0.

Competing interests: The authors declare no competing interests.

References

Angelova MI, Dimitrov DS. 1986. Liposome Electro formation. *Faraday Discuss Chem SOC* **81**:303–311. doi:10.1039/dc9868100303

Antonny B, Madden D, Hamamoto S, Orci L, Schekman R. 2001. Dynamics of the COPII coat with GTP and stable analogues. *Nature Cell Biology* **3**:531–537. doi:10.1038/35078500

Bacia K, Futai E, Prinz S, Meister A, Daum S, Glatte D, Briggs JAG, Schekman R. 2011. Multibudded tubules formed by COPII on artificial liposomes. *Sci Rep* **1**:17. doi:10.1038/srep00017

Barlowe C, Orci L, Yeung T, Hosobuchi M, Hamamoto S, Salama N, Rexach MF, Ravazzola M, Amherdt M, Schekman R. 1994. COPII: a membrane coat formed by Sec proteins that drive vesicle budding from the endoplasmic reticulum. *Cell* **77**:895–907.

Bi X, Corpina RA, Goldberg J. 2002. Structure of the Sec23/24-Sar1 pre-budding complex of the COPII vesicle coat. *Nature* **419**:271–277. doi:10.1038/nature01040

Bi X, Mancias JD, Goldberg J. 2007. Insights into COPII coat nucleation from the structure of Sec23.Sar1 complexed with the active fragment of Sec31. *Dev Cell* **13**:635–645. doi:10.1016/j.devcel.2007.10.006

Bilinovich SM, Davis CM, Morris DL, Ray LA, Prokop JW, Buchan GJ, Leeper TC. 2014. The C-Terminal Domain of SRA1p Has a Fold More Similar to PRP18 than to an RRM and Does Not Directly Bind to the SRA1 RNA STR7 Region. *Journal of Molecular Biology* **426**:1753–1765. doi:10.1016/j.jmb.2014.01.007

Bonifacino JS, Glick BS. 2004. The Mechanisms of Vesicle Budding and Fusion. *Cell* **116**:153–166. doi:10.1016/S0092-8674(03)01079-1

Boyadjiev SA, Fromme JC, Ben J, Chong SS, Nauta C, Hur DJ, Zhang G, Hamamoto S, Schekman R, Ravazzola M, Orci L, Eyaid W. 2006. Cranio-lenticulo-sutural dysplasia is caused by a SEC23A mutation leading to abnormal endoplasmic-reticulum-to-Golgi trafficking. *Nat Genet* **38**:1192–1197. doi:10.1038/ng1876

Buchan DWA, Jones DT. 2019. The PSIPRED Protein Analysis Workbench: 20 years on. *Nucleic Acids Res* **47**:W402–W407. doi:10.1093/nar/gkz297

Castaño-Díez D, Kudryashev M, Arheit M, Stahlberg H. 2012. Dynamo: A flexible, user-friendly development tool for subtomogram averaging of cryo-EM data in high-performance computing environments. *Journal of Structural Biology* **178**:139–151. doi:10.1016/j.jsb.2011.12.017

Čopič A, Latham CF, Horlbeck MA, D'Arcangelo JG, Miller EA. 2012. ER Cargo Properties Specify a Requirement for COPII Coat Rigidity Mediated by Sec13p. *Science* **335**:1359–1362. doi:10.1126/science.1215909

Dokudovskaya S, Williams R, Devos D, Sali A, Chait BT, Rout MP. 2006. Protease Accessibility Laddering: A Proteomic Tool for Probing Protein Structure. *Structure* **14**:653–660. doi:10.1016/j.str.2006.02.006

Emsley P, Lohkamp B, Scott WG, Cowtan K. 2010. Features and development of Coot. *Acta Crystallogr D Biol Crystallogr* **66**:486–501. doi:10.1107/S0907444910007493

Fath S, Mancias JD, Bi X, Goldberg J. 2007. Structure and organization of coat proteins in the COPII cage. *Cell* **129**:1325–1336. doi:10.1016/j.cell.2007.05.036

Fromme JC, Ravazzola M, Hamamoto S, Al-Balwi M, Eyaid W, Boyadjiev SA, Cosson P, Schekman R, Orci L. 2007. The genetic basis of a craniofacial disease provides insight into COPII coat assembly. *Dev Cell* **13**:623–634. doi:10.1016/j.devcel.2007.10.005

Ghaemmaghami S, Huh W-K, Bower K, Howson RW, Belle A, Dephoure N, O'Shea EK, Weissman JS. 2003. Global analysis of protein expression in yeast. *Nature* **425**:737–741. doi:10.1038/nature02046

Gorur A, Yuan L, Kenny SJ, Baba S, Xu K, Schekman R. 2017. COPII-coated membranes function as transport carriers of intracellular procollagen I. *J Cell Biol* **216**:1745–1759. doi:10.1083/jcb.201702135

Grant T, Grigorieff N. 2015. Measuring the optimal exposure for single particle cryo-EM using a 2.6 Å reconstruction of rotavirus VP6. *eLife* **4**:e06980. doi:10.7554/eLife.06980

Hagen WJH, Wan W, Briggs JAG. 2017. Implementation of a cryo-electron tomography tilt-scheme optimized for high resolution subtomogram averaging. *Journal of Structural Biology* **197**:191–198. doi:10.1016/j.jsb.2016.06.007

Hutchings J, Stancheva V, Miller EA, Zanetti G. 2018. Subtomogram averaging of COPII assemblies reveals how coat organization dictates membrane shape. *Nature Communications* **9**:4154. doi:10.1038/s41467-018-06577-4

Hutchings J, Zanetti G. 2019. Coat flexibility in the secretory pathway: a role in transport of bulky cargoes. *Current Opinion in Cell Biology* **59**:104–111. doi:10.1016/j.ceb.2019.04.002

Jin L, Pahuja KB, Wickliffe KE, Gorur A, Baumgärtel C, Schekman R, Rape M. 2012. Ubiquitin-dependent regulation of COPII coat size and function. *Nature* **482**:495–500. doi:10.1038/nature10822

Jones DT, Cozzetto D. 2015. DISOPRED3: precise disordered region predictions with annotated protein-binding activity. *Bioinformatics* **31**:857–863. doi:10.1093/bioinformatics/btu744

Kovtun O, Dickson VK, Kelly BT, Owen DavidJ, Briggs JAG. 2020. Architecture of the AP2:clathrin coat on the membranes of clathrin-coated vesicles. *bioRxiv* 2020.01.28.922591. doi:10.1101/2020.01.28.922591

Kovtun O, Leneva N, Bykov YS, Ariotti N, Teasdale RD, Schaffer M, Engel BD, Owen DJ, Briggs JAG, Collins BM. 2018. Structure of the membrane-assembled retromer coat determined by cryo-electron tomography. *Nature* **561**:561–564. doi:10.1038/s41586-018-0526-z

Kremer JR, Mastronarde DN, McIntosh JR. 1996. Computer visualization of three-dimensional image data using IMOD. *Journal of Structural Biology* **116**:71–76. doi:10.1006/jsbi.1996.0013

Krissinel E, Henrick K. 2007. Inference of macromolecular assemblies from crystalline state. *J Mol Biol* **372**:774–797. doi:10.1016/j.jmb.2007.05.022

Lam SD, Das S, Sillitoe I, Orengo C. 2017. An overview of comparative modelling and resources dedicated to large-scale modelling of genome sequences. *Acta Crystallogr D Struct Biol* **73**:628–640. doi:10.1107/S2059798317008920

914 Lee MCS, Orci L, Hamamoto S, Futai E, Ravazzola M, Schekman R. 2005. Sar1p N-terminal helix initiates
915 membrane curvature and completes the fission of a COPII vesicle. *Cell* **122**:605–617.
916 doi:10.1016/j.cell.2005.07.025
917 Liebschner D, Afonine PV, Baker ML, Bunkóczi G, Chen VB, Croll TI, Hintze B, Hung L-W, Jain S, McCoy
918 AJ, Moriarty NW, Oeffner RD, Poon BK, Prisant MG, Read RJ, Richardson JS, Richardson DC,
919 Sammito MD, Sobolev OV, Stockwell DH, Terwilliger TC, Urzhumtsev AG, Videau LL, Williams
920 CJ, Adams PD. 2019. Macromolecular structure determination using X-rays, neutrons and
921 electrons: recent developments in Phenix. *Acta Cryst D* **75**:861–877.
922 doi:10.1107/S2059798319011471
923 Ma W, Goldberg J. 2016. TANGO1/cTAGE5 receptor as a polyvalent template for assembly of large COPII
924 coats. *PNAS* **113**:10061–10066. doi:10.1073/pnas.1605916113
925 Malhotra V, Erlmann P. 2015. The Pathway of Collagen Secretion. *Annual Review of Cell and*
926 *Developmental Biology* **31**:109–124. doi:10.1146/annurev-cellbio-100913-013002
927 Mastronarde DN. 2005. Automated electron microscope tomography using robust prediction of
928 specimen movements. *Journal of Structural Biology* **152**:36–51. doi:10.1016/j.jsb.2005.07.007
929 Matsuoka K., Orci L, Amherdt M, Bednarek SY, Hamamoto S, Schekman R, Yeung T. 1998. COPII-coated
930 vesicle formation reconstituted with purified coat proteins and chemically defined liposomes.
931 *Cell* **93**:263–275.
932 Matsuoka Ken, Orci L, Amherdt M, Bednarek SY, Hamamoto S, Schekman R, Yeung T. 1998. COPII-
933 coated vesicle formation reconstituted with purified coat proteins and chemically defined
934 liposomes. *Cell* **93**:263–275. doi:10.1016/S0092-8674(00)81577-9
935 Miller E, Antonny B, Hamamoto S, Schekman R. 2002. Cargo selection into COPII vesicles is driven by
936 the Sec24p subunit. *The EMBO Journal* **21**:6105–6113. doi:10.1093/emboj/cdf605
937 Miller EA, Beilharz TH, Malkus PN, Lee MCS, Hamamoto S, Orci L, Schekman R. 2003. Multiple cargo
938 binding sites on the COPII subunit Sec24p ensure capture of diverse membrane proteins into
939 transport vesicles. *Cell* **114**:497–509. doi:10.1016/s0092-8674(03)00609-3
940 Mossessova E, Bickford LC, Goldberg J. 2003. SNARE selectivity of the COPII coat. *Cell* **114**:483–495.
941 Noble AJ, Zhang Q, O'Donnell J, Hariri H, Bhattacharya N, Marshall AG, Stagg SM. 2013. A pseudoatomic
942 model of the COPII cage obtained from cryo-electron microscopy and mass spectrometry.
943 *Nature Structural & Molecular Biology* **20**:167–173. doi:10.1038/nsmb.2467
944 Paraan M, Bhattacharya N, Uversky VN, Stagg SM. 2018. Flexibility of the Sec13/31 cage is influenced
945 by the Sec31 C-terminal disordered domain. *J Struct Biol* **204**:250–260.
946 doi:10.1016/j.jsb.2018.08.016
947 Pettersen EF, Goddard TD, Huang CC, Couch GS, Greenblatt DM, Meng EC, Ferrin TE. 2004. UCSF
948 Chimera - A visualization system for exploratory research and analysis. *Journal of*
949 *Computational Chemistry* **25**:1605–1612. doi:10.1002/jcc.20084
950 Qu K, Glass B, Doležal M, Schur FKM, Murciano B, Rein A, Rumlová M, Ruml T, Kräusslich H-G, Briggs
951 JAG. 2018. Structure and architecture of immature and mature murine leukemia virus capsids.
952 *Proceedings of the National Academy of Sciences* **115**:E11751–E11760.
953 doi:10.1073/pnas.1811580115
954 Saito K, Chen M, Bard F, Chen S, Zhou H, Woodley D, Polischuk R, Schekman R, Malhotra V. 2009.
955 TANGO1 facilitates cargo loading at endoplasmic reticulum exit sites. *Cell* **136**:891–902.
956 doi:10.1016/j.cell.2008.12.025
957 Santos AJM, Nogueira C, Ortega-Bellido M, Malhotra V. 2016. TANGO1 and Mia2/cTAGE5 (TALI)
958 cooperate to export bulky pre-chylomicrons/VLDLs from the endoplasmic reticulum. *J Cell Biol*
959 **213**:343–354. doi:10.1083/jcb.201603072
960 Sikorski RS, Hieter P. 1989. A system of shuttle vectors and yeast host strains designed for efficient
961 manipulation of DNA in Saccharomyces cerevisiae. *Genetics* **122**:19–27.
962 Sillitoe I, Lewis TE, Cuff A, Das S, Ashford P, Dawson NL, Furnham N, Laskowski RA, Lee D, Lees JG,
963 Lehtinen S, Studer RA, Thornton J, Orengo CA. 2015. CATH: comprehensive structural and

964 functional annotations for genome sequences. *Nucleic Acids Res* **43**:D376-381.
965 doi:10.1093/nar/gku947
966 Stagg SM, Gürkan C, Fowler DM, LaPointe P, Foss TR, Potter CS, Carragher B, Balch WE. 2006. Structure
967 of the Sec13/31 COPII coat cage. *Nature* **439**:234–238. doi:10.1038/nature04339
968 Stagg SM, LaPointe P, Razvi A, Gürkan C, Potter CS, Carragher B, Balch WE. 2008. Structural basis for
969 cargo regulation of COPII coat assembly. *Cell* **134**:474–484. doi:10.1016/j.cell.2008.06.024
970 Stancheva VG, Li X-H, Hutchings J, Gomez-Navarro N, Santhanam B, Babu MM, Zanetti G, Miller EA.
971 2020. Combinatorial multivalent interactions drive cooperative assembly of the COPII coat. *J*
972 *Cell Biol* **219**. doi:10.1083/jcb.202007135
973 Terwilliger TC, Ludtke SJ, Read RJ, Adams PD, Afonine PV. 2020. Improvement of cryo-EM maps by
974 density modification. *bioRxiv* 845032. doi:10.1101/845032
975 Townley AK, Feng Y, Schmidt K, Carter DA, Porter R, Verkade P, Stephens DJ. 2008. Efficient coupling of
976 Sec23-Sec24 to Sec13-Sec31 drives COPII-dependent collagen secretion and is essential for
977 normal craniofacial development. *J Cell Sci* **121**:3025–3034. doi:10.1242/jcs.031070
978 Turoňová B, Schur FKM, Wan W, Briggs JAG. 2017. Efficient 3D-CTF correction for cryo-electron
979 tomography using NovaCTF improves subtomogram averaging resolution to 3.4 Å. *Journal of*
980 *Structural Biology* **199**:187–195. doi:10.1016/j.jsb.2017.07.007
981 Venditti R, Scanu T, Santoro M, Di Tullio G, Spaar A, Gaibisso R, Beznoussenko GV, Mironov AA, Mironov
982 A, Zelante L, Piemontese MR, Notarangelo A, Malhotra V, Vertel BM, Wilson C, De Matteis MA.
983 2012. Sedlin controls the ER export of procollagen by regulating the Sar1 cycle. *Science*
984 **337**:1668–1672. doi:10.1126/science.1224947
985 Webb B, Sali A. 2017. Protein Structure Modeling with MODELLER. *Methods Mol Biol* **1654**:39–54.
986 doi:10.1007/978-1-4939-7231-9_4
987 Wiederstein M, Sippl MJ. 2007. ProSA-web: interactive web service for the recognition of errors in
988 three-dimensional structures of proteins. *Nucleic Acids Res* **35**:W407-410.
989 doi:10.1093/nar/gkm290
990 Wuestehube LJ, Schekman RW. 1992. Reconstitution of transport from endoplasmic reticulum to Golgi
991 complex using endoplasmic reticulum-enriched membrane fraction from yeast. *Meth Enzymol*
992 **219**:124–136. doi:10.1016/0076-6879(92)19015-x
993 Zanetti G, Pahuja KB, Studer S, Shim S, Schekman R. 2012. COPII and the regulation of protein sorting
994 in mammals. *Nature Cell Biology* **14**:20–28. doi:10.1038/ncb2390
995 Zanetti G, Prinz S, Daum S, Meister A, Schekman R, Bacia K, Briggs JAG. 2013. The structure of the COPII
996 transport-vesicle coat assembled on membranes. *Elife* **2**:e00951. doi:10.7554/eLife.00951
997 Zheng SQ, Palovcak E, Armache J-P, Verba KA, Cheng Y, Agard DA. 2017. MotionCor2: anisotropic
998 correction of beam-induced motion for improved cryo-electron microscopy. *Nature Methods*
999 **14**:331–332. doi:10.1038/nmeth.4193
1000 Zimmermann L, Stephens A, Nam S-Z, Rau D, Kübler J, Lozajic M, Gabler F, Söding J, Lupas AN, Alva V.
1001 2018. A Completely Reimplemented MPI Bioinformatics Toolkit with a New HHpred Server at
1002 its Core. *Journal of Molecular Biology*, Computation Resources for Molecular Biology **430**:2237–
1003 2243. doi:10.1016/j.jmb.2017.12.007
1004

A

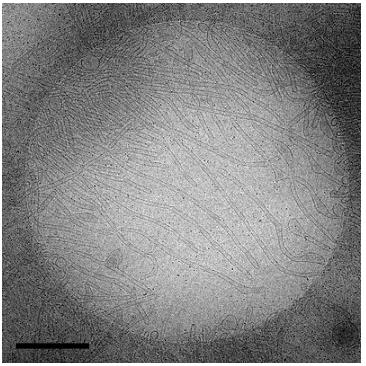

B

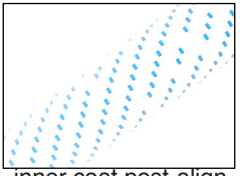

inner coat post-align

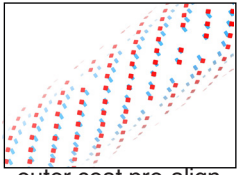

outer coat pre-align

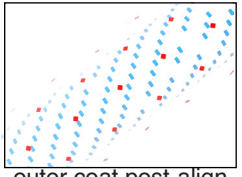

outer coat post-align

C Reference Average

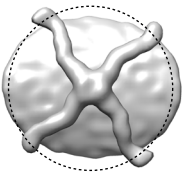

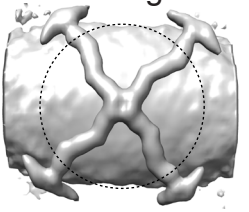

EMD-2429

D

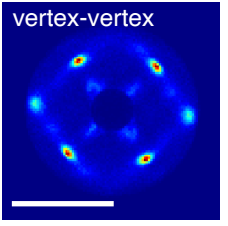

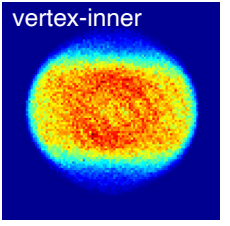

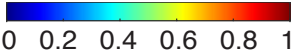

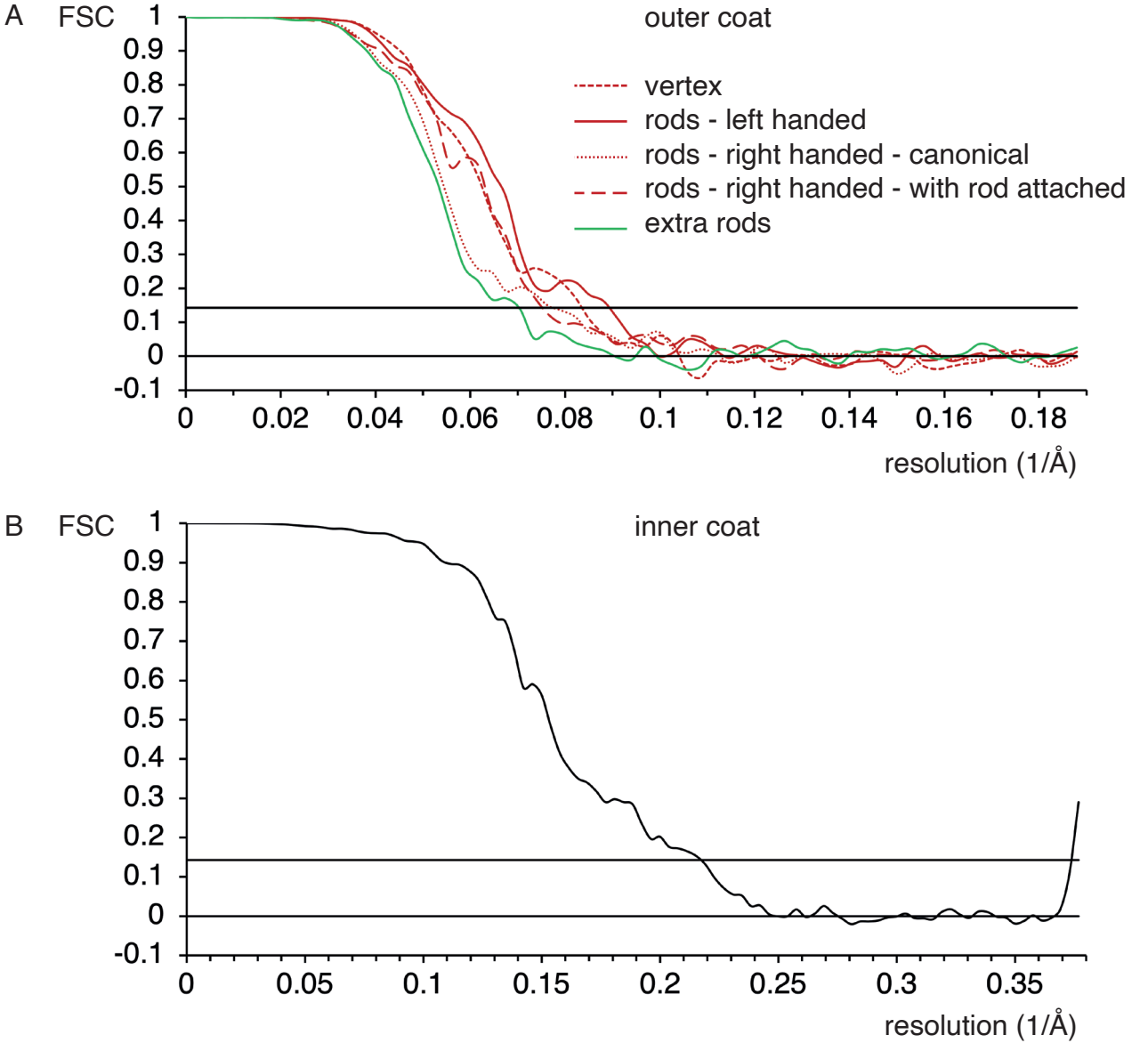
A
FSC
outer coat
vertex
rods - left handed
rods - right handed - canonical
rods - right handed - with rod attached
extra rods
1
0.9
0.8
0.7
0.6
0.5
0.4
0.3
0.2
0.1
0
-0.1
0
0.02
0.04
0.06
0.08
0.1
0.12
0.14
0.16
0.18
resolution (1/Å)
B
FSC
inner coat
1
0.9
0.8
0.7
0.6
0.5
0.4
0.3
0.2
0.1
0
-0.1
0
0.05
0.1
0.15
0.2
0.25
0.3
0.35
resolution (1/Å)

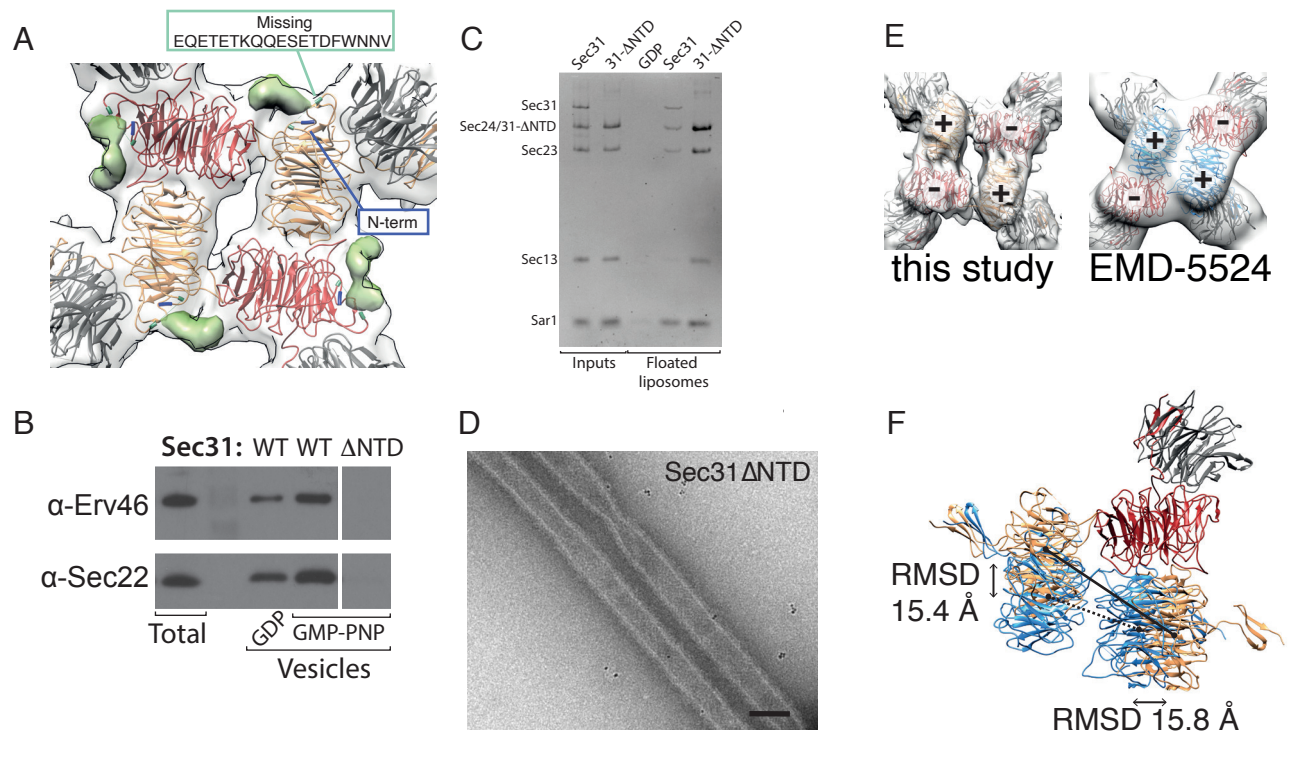
A
Missing
EQETETKQQESETDFWNNV
N-term
C
Sec31
31-ΔNTD
GDP
Sec31
31-ΔNTD
Sec31
Sec24/31-ΔNTD
Sec23
Sec13
Sar1
Inputs
Floated liposomes
E
this study
EMD-5524
B
Sec31: WT WT ΔNTD
α-Erv46
α-Sec22
Total
GDP
GMP-PNP
Vesicles
D
Sec31ΔNTD
F
RMSD 15.4 Å
RMSD 15.8 Å

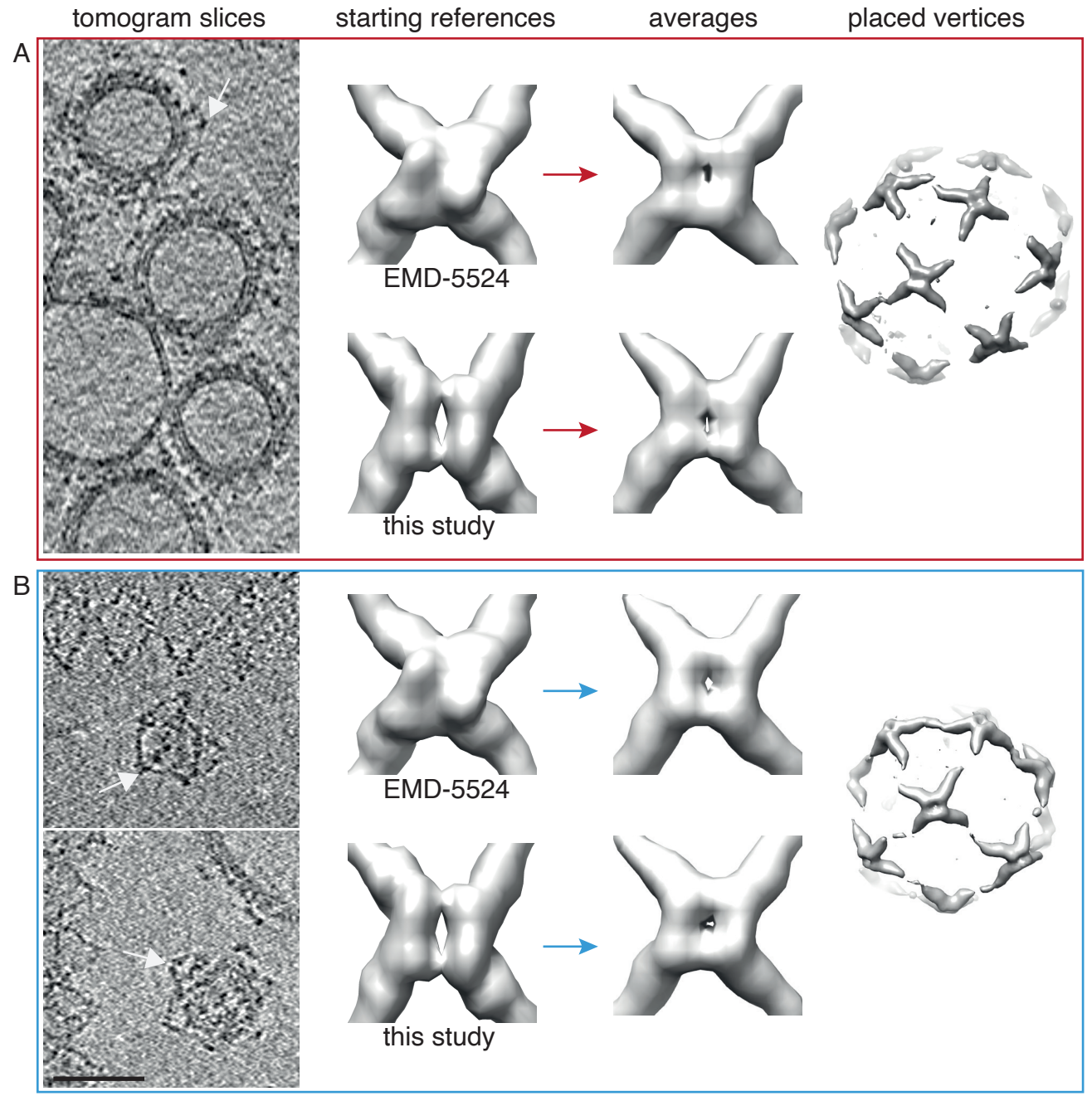
tomogram slices
starting references
averages
placed vertices
A
EMD-5524
this study
B
EMD-5524
this study

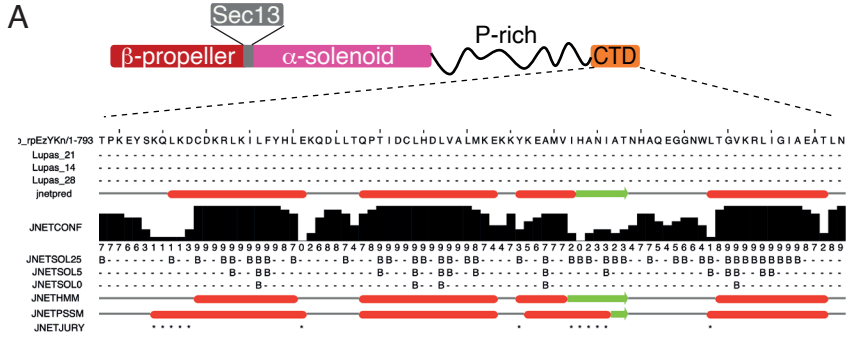
A
Sec13
β-propeller
α-solenoid
P-rich
CTD
Lupas_21
Lupas_14
Lupas_28
jnetpred
JNETCONF
JNETSOL25
JNETSOL5
JNETSOL0
JNETHMM
JNETPSSM
JNETJURY

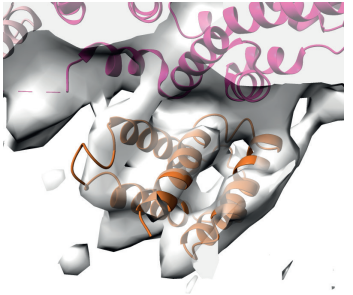
B

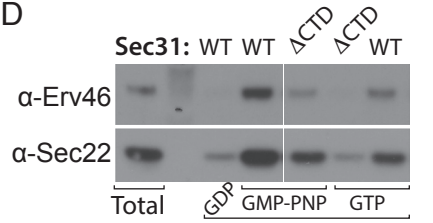
D
Sec31: WT WT ΔCTD ΔCTD WT
α-Erv46
α-Sec22
Total
GDP
GMP-PNP
GTP
Vesicles

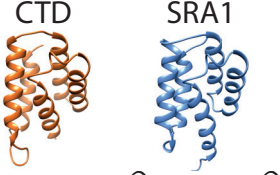
C
CTD
SRA1

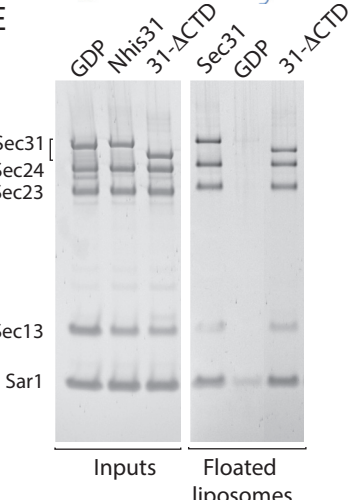
E
GDP
Nhis31
31-ΔCTD
Sec31
GDP
31-ΔCTD
Sec31
Sec24
Sec23
Sec13
Sar1
Inputs
Floated liposomes

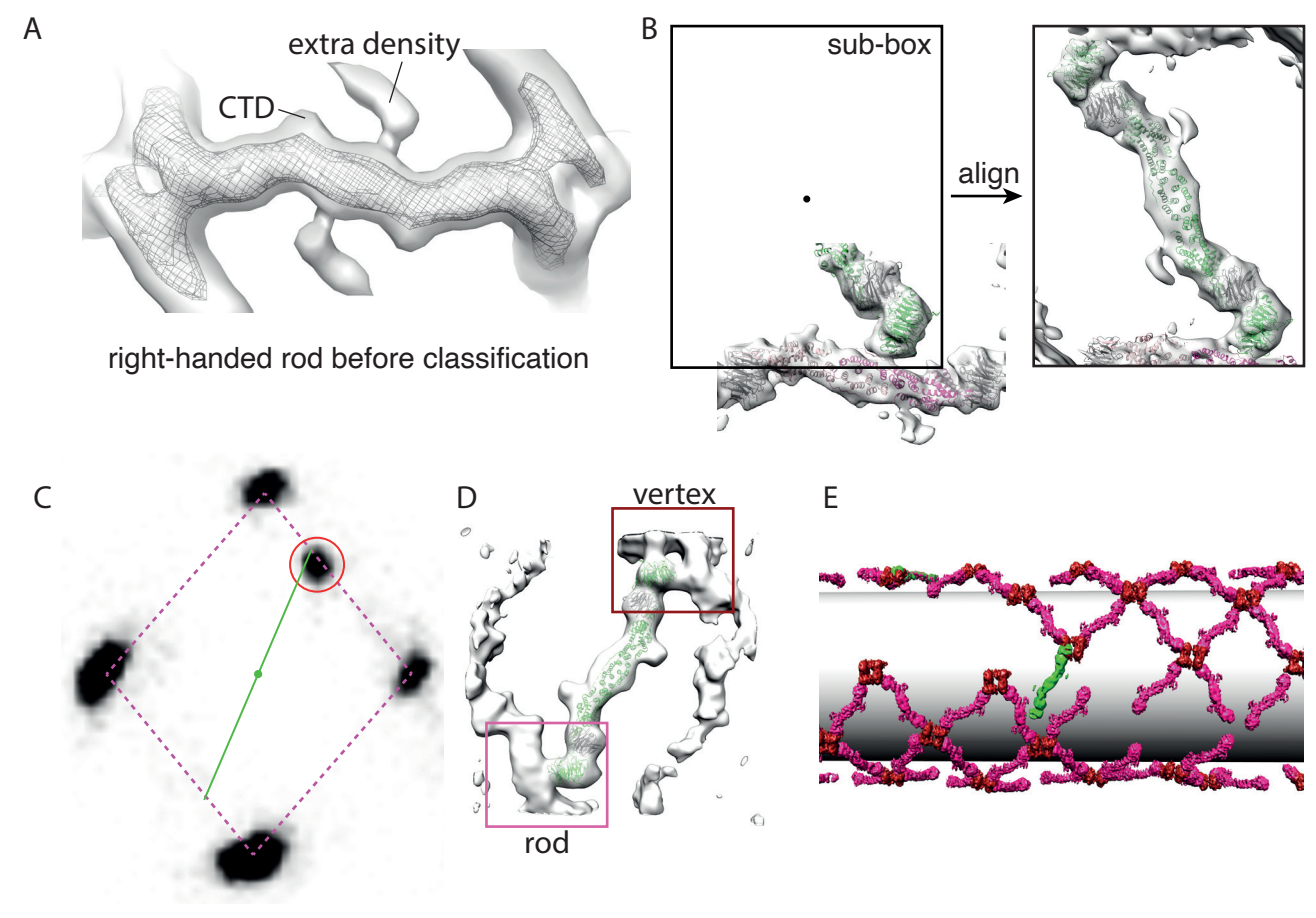
A
extra density
CTD
right-handed rod before classification
B
sub-box
align
C
D
vertex
rod
E

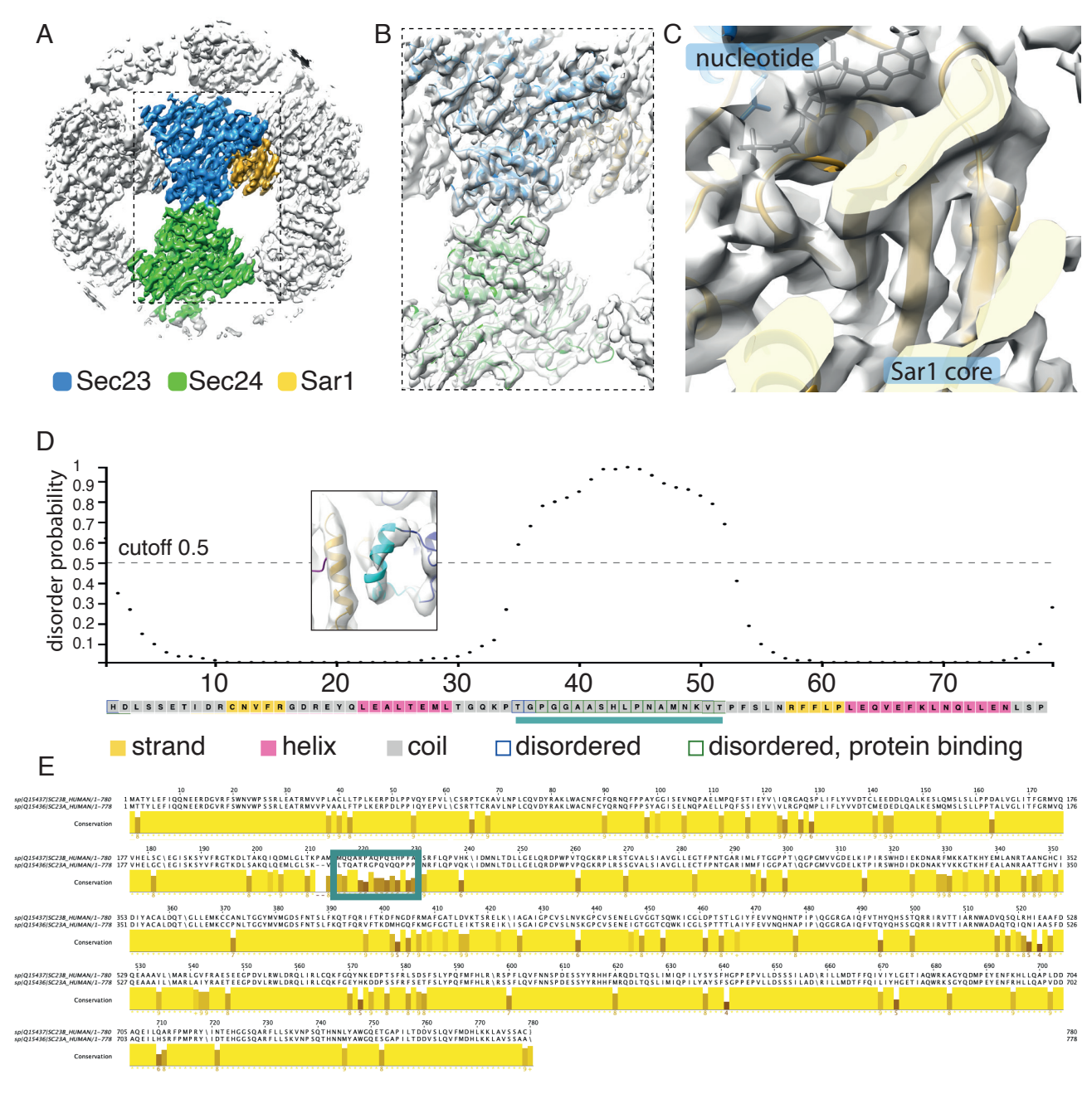
A
B
C
nucleotide
Sar1 core
Sec23
Sec24
Sar1
D
disorder probability
cutoff 0.5
strand
helix
coil
disordered
disordered, protein binding
E
Conservation